

Reviewer#1:

Based on model simulations and recent satellite observations, the authors examine the skill of high resolution WRF on the impact of snow albedo darkening on radiative forcing. They evaluate the model simulation with various observations. The authors also discussed the benefit of high resolution model, by comparing with coarser resolution model simulation, in aerosol and snowpack distribution over HMA. Lastly, spatial/temporal variation of radiative response are also discussed. This is well organized and clearly written manuscript. I would like to suggest this work for publication subject to a revision to address following concerns.

Response: We are grateful to the reviewer for the thorough reading and insightful comments on our manuscript. We have addressed all the comments and suggestions provided by the reviewer. Our point-by-point responses for the specific comments are mentioned below in blue color.

The subsequent modifications and additions in our revised manuscript are shown in red color.

1) Snow albedo: How was snow albedo estimated when snow cover fraction is less than 1? For example, is albedo difference between WRF-HR and WRF-CR (Fig. 5) due to snow cover fraction or aerosol concentration (LAP)? If snow cover fraction is an important factor, can model snow albedo be compared with STC-MODDRFS?

Response: We thank the reviewer for this suggestion. Simulated annual mean “snow albedo” values are primarily the composite albedo values of snow covered grids. In WRF-Chem-SNICAR simulations, the composite albedo of a snow-covered grid box is computed as weighted average of representative area fractions of sub-grid snow-cover and snow-free regions. Thus, snow cover fraction is indeed a contributor to the differences in the surface albedo estimations between the two simulations. However, the differences in the annual/seasonal mean snow albedo values (between WRF-HR and WRF-CR) is resultant of differences in several other factors also i.e. the snow grain size and associated evolution, LAP concentration and snow duration. As discussed in the manuscript, better representation of terrain elevation in WRF-HR (via high spatial resolution) run brought synergistic improvement in all these factors and improves the simulation of albedo over snow-covered grids.

We have included the following discussion about contribution of snow fraction in our comparison of Figure 5 (snow albedo) in the revised manuscript at Line nos 492-513.

The improvement of α estimation in WRF-HR runs compared to WRF-CR runs can be attributed to the relatively better simulation of fSCA (Figure 2), NSD (Figure 3) and SGS (Figure 4) in WRF-HR. Simulated annual mean α values are primarily the composite albedo values of snow covered grids. In WRF-Chem-SNICAR simulations, the composite albedo of a snow-covered grid box is computed as weighted average of representative area fractions of sub-grid snow-cover and snow-free regions. Thus, relatively lower values of simulated fSCA and NSD in

WRF-CR runs compared to WRF-HR runs can contribute substantially to the relatively lower annual and seasonal mean α values simulated by WRF-CR.

At the same time, the mean α values from STC-MODSCAG (representative of only snow covered regions) are biased towards higher values than the corresponding simulated α values (composite albedo of the pixel) predominantly over the snow grids with annual mean fSCA are much smaller than 1.

2) Season: Winter and summer are defined as DJF and AMJ in main text while NDJF and MAMJ are used in supplementary material. Spring is more appropriate for AMJ as well as MAMJ.

Response: We have replaced “summer” with “pre-monsoon” in the revised manuscript and have also corrected the information in supplementary material.

3) Line 336: 16:00LT → 14:00LT

Response: We have corrected this mistake.

4) Validation of LAP (Lines 362-370): What would be the effect of using LAP data observed in different year and different glaciers?

Response: We have added the following sentences in revised manuscript at Line numbers 328-335 to discuss this issue.

We understand that use of measurements from a year different than 2013-14 would introduce error in our evaluation. Moreover, simulated annual mean LAP concentration from the topmost snow surface layer (only) is compared to the observed surface snow LAP concentration. This might also introduce differences in the snow sampling depth in our evaluation. However, we have used more than one study to have a range of annual mean LAP values over each location so in principle the observations are representative of different years and different snow depths over the same glacier. Also, to minimize the influence of snow sample depth variation, we have only used data in the literature which are observed as snow surface measurement or from snow pits having a thickness less than 15 cm.

5) Lines 416-418: It seems obvious, but any thought why model overestimate snow cover fraction in DJF and underestimate in AMJ? Does model simulate reasonable surface temperature and precipitation over the region?

Response: We thank the reviewer for this suggestion. We analyzed the simulated spatial and temporal variation in surface rainfall (as a proxy for surface precipitation) and found that WRF-HR indeed overestimates precipitation, which can contribute to the overestimation of simulated fSCA as well as affect the surface temperature. Accordingly, we have added the

following figure in supplementary and sentences at Line number 387-390 in the revised manuscript.

Further, WRF-HR simulated annual surface rainfall in winter is overestimated over Karakoram, Himalayan and Hindukush ranges (Figure S3). This indicates that overestimation of surface precipitation in WRF-HR may also contribute to the overestimation of fSCA over HMA in winter.

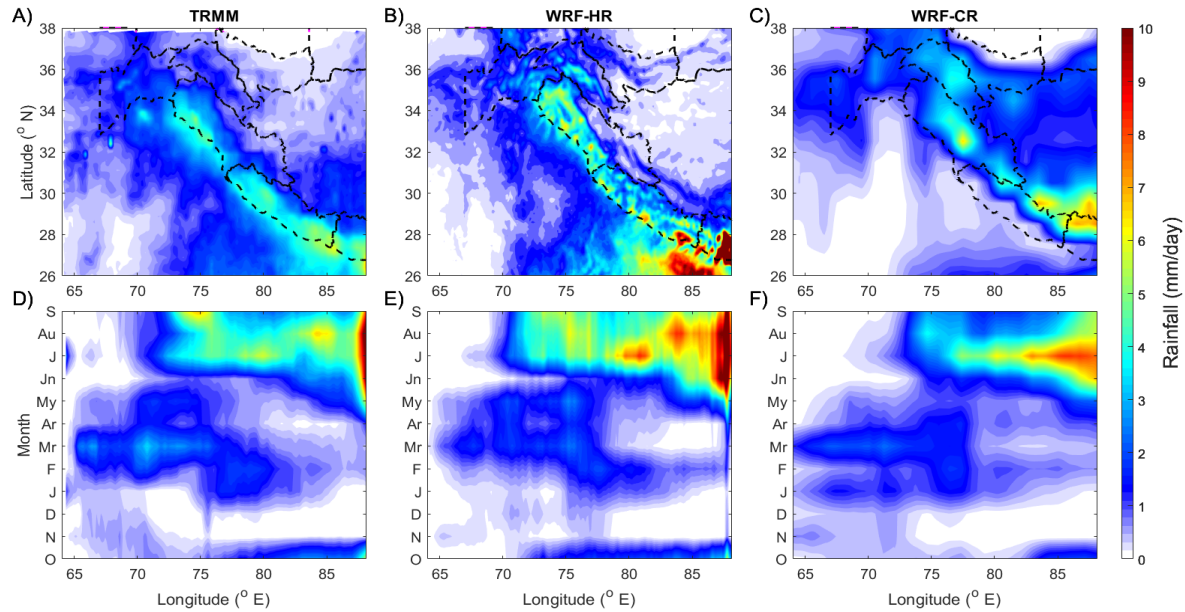


Figure S3: Spatial distribution of annual mean surface precipitation (in mm/day) for water year 2013-14 from A) TRMM satellite, B) WRF-HR and C) WRF-CR simulations are shown. Corresponding Time-Longitude distribution of latitudinal-mean rainfall is also shown in Panels D-F, respectively.

6) Line 461: Is “and 4F” typo?

Response: Yes, we have corrected this mistake.

7) Lines 498-503: Hard to read. Are “13” and “14” day of the month?

Response: Here, 13 and 14 meant 2013 and 2014. We have revised the sentences accordingly to replace “13” and “14” with “2013” and “2014”, respectively, in that paragraph for clarity.

8) Lines 509-512: It’s hard to follow the argument. Would you get the same conclusion if a different grid is used?

Response: Figures 4 show that snow grain size (SGS) values over the HMA region are better simulated in WRF-HR runs compared to WRF-CR runs. An anomaly to this feature is seen over a few grids in western Himalaya, where, the WRF-CR simulated SGS values are closer to

observations than that simulated in WRF-HR. The fSCA-SGS association over these specific grids is discussed in Figure 4E to understand this anomaly. We illustrate that the model biases in simulated SGS values are mainly proportional to the corresponding biases in fSCA and NSD, which is valid for all grids across the HMA region.

We have rephrased the paragraph at Line numbers 463-481 as below for more clarity.

Quite anomalous to other grids in HMA, the WRF-CR simulated SGS values over some grids near the Chotta Shingri glacier (marked by magenta circle in Figure 4A) of the western Himalaya sub-region are closer to STC-MODSCAG observations than that simulated by WRF-HR runs. As a sanity check, daily variation of SGS (hashed lines in Figure 4E) and fSCA (solid lines in Figure 4E) from STC-MODSCAG (black), WRF-HR (blue) and WRF-CR (red) over this glacier are compared. Fractional snow cover from STC-MODSCAG gradually increase from 0.2 in November, 2013 to 0.8 in February, 2014 and subsequently decrease back to 0.1 by September, 2014 at the glacier location. Corresponding SGS values from STC-MODSCAG closely followed the seasonal trend in fSCA varying around the values of 80-200 micron in winter. In comparison, simulated fSCA from WRF-HR values drastically increased to 1 at the beginning of November, 2013 (from no snow cover before that), remained fully snow covered till mid-June, 2014 and then suddenly became snow free after June. Compared to satellite estimates, fSCA from WRF-HR are greater in magnitude throughout the duration of snow cover indicating more snow mass simulated by WRF-HR. Associated SGS values (80-800 micron) simulated by WRF-HR are also greater than STC-MODSCAG estimates throughout the snow duration over the grid. However, the fSCA variation from WRF-CR over this grid is very close to the variation seen by STC-MODSCAG, and the associated SGS values (50-400 micron) from WRF-CR are also closer to the estimated STC-MODSCAG values, supporting our argument that biases in simulation of fSCA also affect the simulated annual mean SGS values.

9) Line 515: Fig. 4 → Fig. 5

Response: Yes, we have corrected this mistake.

10) Fig. 4 has a wrong caption

Response: Yes, we have corrected this mistake.

11) Fig. 5 has a wrong caption

Response: Yes, we have corrected this mistake.

12) Fig. 7A: What cause the high LAP in the south of Taklamakan desert?

Response: Local dust emissions and dust transported from Taklimakan desert is the source of LAP concentration in snow over the HMA ranges to the south of Taklimakan desert. Moreover, improvement in fractional snow cover (Figure 2B and 2C) and snow duration (Figure 3B and 3C)

over the entire stretch of HMA ranges to the south of Taklimakan desert is also seen in WRF-HR runs (compared to WRF-CR runs). Thus, longer duration of snow cover and greater dust deposition in WRF-HR (Figures S6, S7) result in higher annual mean LAP values than WRF-CR runs.

13) Spatial pattern of LAP (Fig. 7) doesn't seem to highly correlated with albedo (Fig. 5)

Response: Annual mean snow albedo spatial pattern is primarily governed by spatial pattern and frequency of snowfall, snow grain size evolution and associated aging, LAP concentration and the snow pack duration. In contrast, the annual mean spatial pattern of LAP concentration in snow is governed by aerosol emission, transport and meteorology/terrain induced deposition of aerosols to the snow packs and snow cover duration. Inherent differences in these governing factors results in these two variables not being highly correlated spatially over HMA. Secondly, the LAP concentration is higher at lower elevations, but comparatively snow albedo values are greater at higher elevations. Thirdly, more LAP concentration itself decreases the snow albedo values, making these two variables anti-correlated within the same grid.

14) AOD is higher in CR, but LAP is higher in HR. Yet, albedo is higher in HR in general. It is probably due to higher snow cover (See also my comment #1) and more snowfall (Lines 654-657) in HR. If so, additional simulation (with similar climatology) may be required to discuss the impact of snow darkening.

Response: AOD is the measure of particles airborne in model atmosphere layers. LAP in snow is the measure of particles deposited in the surface snow layer of the model. The lifetime of airborne aerosols and deposition of airborne aerosols to snow packs is dependent on precipitation (wet deposition) and terrain (dry deposition). Greater snowfall and greater terrain heights over HMA are simulated in WRF-HR (compared to coarser resolution runs), which enhances the total deposition flux of aerosols into snow packs. This results in relatively higher LAP in snow surface (but lower lifetime and AOD) over HMA than that simulated in WRF-CR (Figures 7 and 8 and Figures S6-S7). As replied to comment #1, the differences in simulation of many factors i.e. aerosol emissions, transport, meteorology, fSCA, and snow microphysical properties all contributes to the differences in AOD and LAP better WRF-HR and WRF-CR.

The differences in LAP-induced snow albedo darkening (between WRF-HR and WRF-CR) is primarily governed by the LAP concentration in top snow layer. Larger LAP concentration can induce more snow darkening. The comparisons presented in our manuscript clearly show the improvement in WRF-HR simulated LAP concentration in snow and thus argue that higher spatial resolution will bring improvement in simulation of LAP-induced snow albedo darkening. Considering that meteorology itself, including precipitation, is coupled to the terrain elevation over HMA, meteorological conditions seldom remains constant (to manifest similar climatology) while studying the effect of spatial resolution on aerosol-snow interactions. Our study is meant to study such effect of model resolution in the coupled atmosphere-snow-terrain system with all the interactions considered in a consistent manner.

15) Fig. 9C & Lines 866-868: What cause the bias? Does model has local source of dust over HMA?

Response: The biases in WRF-HR simulated LAP-induced snow darkening in winter in comparison to the STC-MODDRFS estimates (Fig. 9C and Lines 866-868) is mainly attributable to uncertainty in simulation of snow layer properties (fSCA, NSD, SGS), aerosol emission, distribution, transport and deposition (AOD, LAP, meteorology) and various inherent assumptions within the model parameterization towards representation of snow morphology and LAP-snowmelt dynamical feedbacks in our model.

Yes, our model has local sources of dust over HMA (see Figure R1 in comment #16). Following Zhoa et al., 2010, the dust emission scheme adopted from the Goddard Chemistry Aerosol Radiation and Transport (GOCART) model (Ginoux et al., 2001) coupled with the MOSAIC aerosol schemes is used in this study. GOCART dust emission parameterization is dependent on near surface wind speed. Previous studies have evaluated this parameterization and illustrated inherent uncertainties, mostly underestimation over Indian region (Dipu et al., 2013; Kumar et al., 2014). Thus, the uncertainty in local dust emissions (along with other factors) can also contribute to the biases in simulated $\Delta\alpha$ values. We thank the reviewer for directing us towards this uncertainty.

We thank the reviewer for this comment about local dust emissions. We have included a discussion focused on all the uncertainties involved in simulated LAP-induced snow darkening in the revised manuscript at Line numbers 676-728.

As already discussed, the simulated fSCA values in WRF-HR are greater than observed fSCA from STC-MODSCAG for most of the winter season. Specifically, the underestimation in WRF-HR simulated $\Delta\alpha$ values (Figures 9C and 9D) in winter over Karakoram, Hindu Kush and Himalayas is in agreement with corresponding overestimation of WRF-HR simulated fSCA values over these regions (Figure 2). STC-MODDRFS estimated $\Delta\alpha$ is based on surface reflectance, while $\Delta\alpha$ calculated by model involves the surface layer depth. The surface snow layer in SNICAR/CLM continuously evolves as fresh snowfall is added or with snow melting, so the LAP concentrations in the surface layer depend on new snowfall, meltwater flushing, and layer combination/division (Flanner et al., 2007; Flanner et al., 2012; Oleson et al., 2010). Therefore, more precipitation and more snow coverage in winter can be a primary factor causing the underestimation of annual mean LAP concentration and LAP-induced snow darkening. Secondly, the associated overestimation in simulated SGS during winter (Figure 4E) can also contribute to the lower $\Delta\alpha$ values simulated in WRF-HR because bigger snow grains in WRF-HR lead to lower clean albedo and thus smaller percentage reduction in albedo compared to STC-MODDRFS. Moreover, we have assumed spherical shaped snow grains in our simulations. Recently, microscopic level studies show that uncertainties associated with simplified snow grain shape treatment in model parameterization can solely contribute to large biases in SNICAR- $\Delta\alpha$ estimates and thus the LAP-snow albedo radiative and snow melt feedback processes (Liou et al., 2014; Dang et al., 2016; He et al., 2017). Thirdly, the fact that the

persistent cloud cover over HMA during winter season can induce a lot of uncertainty in the STC-MODSCAG and STC-MODDRFS estimates, is also equally important.

At the same time, uncertainties regarding aerosol emission, transport and deposition to the snow layers are also significant. It is well known that the transport and deposition of black carbon from Indian landmass to Himalayas increases in the afternoon with the evolution of boundary layer over the IGP region (Dumka et al., 2015; Raatikainen et al., 2014). This feature is well simulated by the model (not shown). As STC-MODDRFS estimates are representative of 1000 LT, but simulated values are sampled in the midday (1000-1400 LT), positive biases in aerosol transport and deposition in snow packs (i.e. higher $\Delta\alpha$ values) might be simulated in WRF-HR runs, especially during pre-monsoon months. At the same time, GOCART dust emission parameterization (used here) is dependent on near surface wind speed. Previous studies have evaluated and illustrated inherent uncertainties in dust emission by this parameterization, mostly underestimation over Indian region (Dipu et al., 2013; Kumar et al., 2014). Thus, the uncertainty in local dust emission fluxes over HMA can also contribute to the biases in simulated $\Delta\alpha$ values. Also, large biases in LAP values may be simulated due to model uncertainties in enhanced wet scavenging fluxes in winter. An overestimation in LAP concentration can lead to an overestimation of snow darkening and melting, resulting in an underestimation of NSD (Figure S4). The large biases in $\Delta\alpha$ values (> 20 %) simulated by WRF-HR towards late spring could be attributed to both, underestimation in fSCA and overestimation of LAP concentration in the model.

Although a better quantification of these model biases requires evaluation against in-situ measurements, it is worth mentioning here that no in-situ measurements are available for a direct comparison of these high $\Delta\alpha$ values WRF-HR over W. Himalayas (Gertler et al., 2016). Nonetheless, the high values simulated during pre-monsoon are close to previously reported values over other HMA regions. Kaspari et al., (2014) used the offline SNICAR model to report that BC concentrations in pre-monsoon snow/ice samples at Mera Glacier were large enough to reduce albedo by 6-10% and the reduction in albedo was 40-42% relative to clean snow when dust is included in the calculation. Recently, Zhang et al. (2018) has combined a large dataset of LAP measurements in surface snow with the offline SNICAR model to illustrate that $\Delta\alpha$ can be >35% over Tibetan Plateau. Moreover, the composite effect of this discrepancy on seasonal/annual mean values is minimal as the snowpack is at its minimum near the end of pre-monsoon season. Similar high daily variability, huge radiative forcing values (LAPRF ~ 200 W/m²) and sudden decline in snow depth in late pre-monsoon is also reported over upper Colorado river basin (Skiles et al., 2015; Skiles and Painter, 2017)

16) Same emission databases on relatively coarse resolution are used for both simulations. How about actual emission of dust and BC? Are they comparable in HR and CR?

Respond: We agree with the reviewer that there is uncertainty in the emission rates we used in our simulations. Real-world fugitive emissions are still not accounted in coarsely resolved inventories which can indeed induce uncertainty in our simulations. Moreover, scarcity in

three-dimensional measurements have limited certainty analysis of various global inventories over Asia including HMA region. Nonetheless, the main objective of our study is to illustrate the impact of horizontal resolution on aerosol, LAP and snow properties via improved terrain representation, so we have kept the emission inventories same for both the runs, WRF-HR and WRF-CR. Although, dust emissions in both HR and CR runs vary as it depends on simulated meteorology (Figure R1), the emission fluxes are comparable over HMA. The black carbon emission fluxes used in both HR and CR runs are also comparable (same anthropogenic emission inventory).

We included the following sentence in the revised manuscript at Line number 555.

Moreover, Jayarathne et al., 2018 shows that many local emissions are not accounted in coarse emissions which causes underestimation in simulated regional AOD values in these valleys.

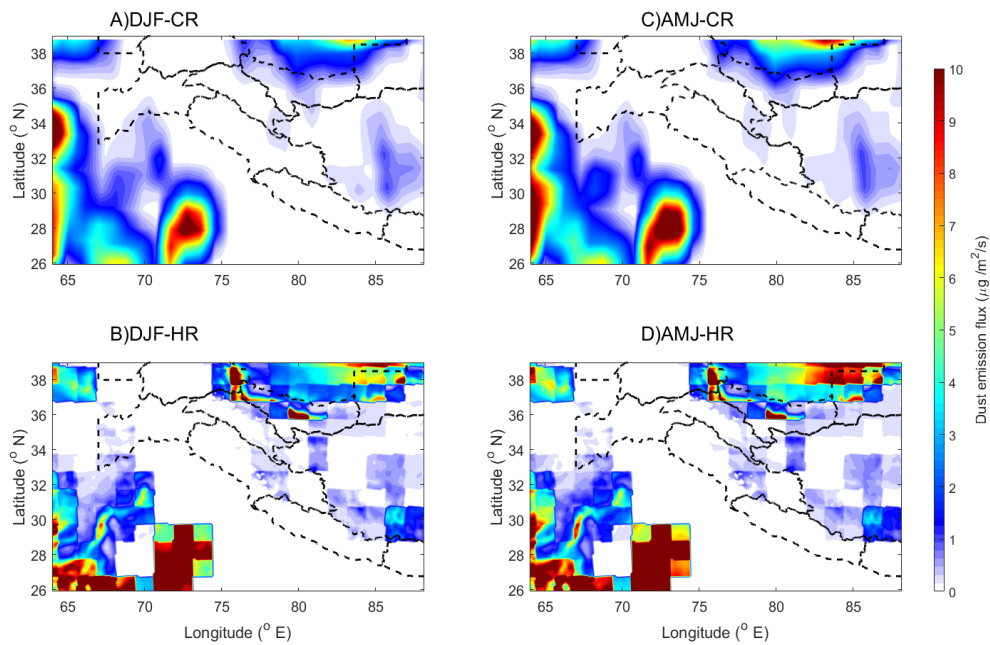


Figure R1: Spatial distribution of mean deposition rate for A) WRF-CR runs and B) WRF-HR during winter months. Panel C) and D) are same as Panels A) and B), but, for pre-monsoon months.

Reviewer#2

This study performed WRF-Chem high-resolution (~12km) model simulations coupled with the SNICAR model to resolve BC/dust-snow interactions and associated albedo reductions. The model results are evaluated with a suite of observations for snow properties and aerosol conditions. The authors further illustrated the effect of model resolution by comparing with a quasi-global WRF-Chem simulation. This study highlights the importance of model resolution and aerosol-snow interactions in modeling the Tibetan Plateau hydroclimate. The manuscript is generally well-organized and well-written. I have a few comments and suggestions to help improve the manuscript.

Response: We are thankful to the reviewer for the positive comments and helpful suggestions. We have addressed all the suggestions and our point-by-point responses for the specific comments are mentioned below in blue color.

The subsequent modifications and additions in our revised manuscript against each comment are shown in red color.

1. When evaluating modelled LAP concentration in snow, did the authors average the LAP concentrations throughout all the snow layers (up to 5) in the model? Or did the authors only look at specific snow thickness (e.g., top 10 cm) in the model? The observed LAP in surface snow may have different sampling thicknesses/depths. More clarifications could be useful. Similar clarifications should also be provided for snow grain size calculations and evaluation.

Response: In our study, simulated values of LAP concentration and snow grain size from the topmost snow layer are compared to the observed values.

In Figure 7, we show the comparison of simulated annual mean LAP values (circle) and simulated range of midday mean LAP values (box plot) against a range of annual mean LAP measurements from literature (obtained from more than one study over each location). The top layer estimates of LAP in snow depends on meltwater flushing, new snowfall and associated top layer evolution (Flanner et al., 2007, 2012; Oleson et al., 2010). Thus, the snow layer corresponding to LAP concentrations varies daily. At the same time, the corresponding range in measurements (annual mean LAP values) used here (except Pamirs) is in principle representative of different years and different snow depths over a location. We agree with the reviewer that the observed LAPs in surface snow have different sampling depths. To minimize the influence of snow sampling depth variation, we have only used the data from literature which are observed as snow surface measurement or from snow pits having thickness less than 15 cm. Additionally, as our model grid size has spatial resolution of 12 km, it is reasonable to believe that other factors like meteorology conditions, AOD distribution, microphysical parameterizations of LAP-snowmelt association and macrophysics of the simulated snow packs can impose greater biases to our simulated annual mean LAP concentration compared to this

discrepancy in snow sample depth. The satellite based observations of snow grain size from STC-MODSCAG data is representative of the snow surface layer. Therefore, we have used the corresponding model values from top snow layer in snow grain size comparisons.

We have added the following discussions on this uncertainty in the methodology section of revised manuscript and also modified Figure 7 caption for better clarity.

Line numbers: 157-161

Note that the number of snow layers and thickness of top snow surface layer are predicted in the CLM model. Fresh snowfall and melting continuously affect the model surface snow layer thickness (3 cm or less). Therefore, LAP concentrations within each snow layer depend on meltwater flushing, new snowfall and associated top layer evolution (Flanner et al., 2007, 2012; Oleson et al., 2010).

Line number: 305

Simulated SGS values from the topmost snow surface layer is compared to the MODSCAG SGS retrievals.

Line number: 328-335

We understand that use of measurements from a year different than 2013-14 would introduce error in our evaluation. Moreover, simulated annual mean LAP concentration from the topmost snow surface layer (only) is compared to the observed surface snow LAP concentration. This might also introduce differences in the snow sampling depth in our evaluation. However, we have used more than one study to have a range of annual mean LAP values over each location so in principle the observations are representative of different years and different snow depths over the same glacier. Also, to minimize the influence of snow sample depth variation, we have only used data in the literature which are observed as snow surface measurement or from snow pits having a thickness less than 15 cm.

2. Introduction (Lines 112-114): For the authors' information, there are a number of valuable recent global modeling studies on the LAP-induced snow albedo effect over the Tibetan Plateau which could be included here as references (e.g., Kopacz et al. 2011 ACP, <https://doi.org/10.5194/acp-11-2837-2011>; He et al. 2014 GRL, <https://doi.org/10.1002/2014GL062191>; Zhang et al. 2015 ACP, <https://doi.org/10.5194/acp-15-6205-2015>).

Response: We thank the reviewer for this information. We have included these and other latest studies in our revised manuscript. The modified text is at Line numbers 65-70.

Many of these studies used online global model simulations at coarse spatial resolutions of ~50-150 km (Flanner and Zender, 2005; Ming et al., 2008; Qian et al., 2011; Kopacz et al., 2011; Zhang et al., 2015). Other studies employed offline simulation of the snow albedo effect using measured or modelled concentrations of deposited LAP in surface snow or estimated from atmospheric loading and ice cores (Yasunari et al., 2013; Nair et al., 2013; Wang et al., 2015; He et al., 2014; Santra et al., 2019).

3. Line 343: It is a little weird to identify April-June as the summer season. How about using “pre-monsoon” season?

Response: We have replaced “summer” with “pre-monsoon” in the revised manuscript.

4. Is there any specific reason to select 2013-2014 water year as the simulation period? Is it because the availability of observations?

Response: In the NASA’s HMA project, the water year 2013-2014 is identified as a good water year for study. Therefore, we selected this year for satellite retrieval and model simulations.

5. Another important uncertainty factor the authors did not mention is the snow grain shape effect. Recent studies have shown significant effects from nonspherical snow grain shapes on snow albedo and BC/dust-induced albedo reduction (e.g., Liou et al. 2014 JGR, <https://doi.org/10.1002/2014JD021665>; Dang et al. 2016 JAS, <https://doi.org/10.1175/JAS-D-15-0276.1>; He et al. 2017 JC, <https://doi.org/10.1175/JCLI-D-17-0300.1>). I suggest including some discussions on this aspect. Also, did the authors assume spherical snow grains in their model simulations? This should be clarified in the model description.

Response: Yes, we have assumed spherical shaped snow grains in the simulations. In agreement with this suggestion from the reviewer, we have revised our manuscript to include the references and a discussion on the uncertainties in simulated aerosol-induced snow albedo darkening due to snow grain shape assumption.

The modified text is added at Line number 690-695 in the revised manuscript is shown below.

Moreover, we have assumed spherical shaped snow grains in our simulations. Recently, microscopic level studies show that uncertainties associated with simplified snow grain shape treatment in model parameterization can solely contribute to large biases in SNICAR- $\Delta\alpha$ estimates and thus the LAP-snow albedo radiative and snow melt feedback processes (Liou et al., 2014; Dang et al., 2016; He et al., 2017).

6. It would be useful if the authors could add a section to discuss the uncertainties involved in this study for the estimates of aerosol-induced snow albedo effects. For example, uncertainties from overestimated fSCA and SGS, underestimated NSD, AOD biases, etc

Response: Following this suggestion from the reviewer, we have included a focused discussion on the uncertainties involved in simulated LAP-induced snow albedo darkening.

The modified text is added at Line number 676-728 in the revised manuscript is shown below.

As already discussed, the simulated fSCA values in WRF-HR are greater than observed fSCA from STC-MODSCAG for most of the winter season. Specifically, the underestimation in WRF-HR simulated $\Delta\alpha$ values (Figures 9C and 9D) in winter over Karakoram, Hindu Kush and Himalayas is in agreement with corresponding overestimation of WRF-HR simulated fSCA values over these regions (Figure 2). STC-MODDRFS estimated $\Delta\alpha$ is based on surface reflectance, while $\Delta\alpha$ calculated by model involves the surface layer depth. The surface snow layer in SNICAR/CLM continuously evolves as fresh snowfall is added or with snow melting, so the LAP concentrations in the surface layer depend on new snowfall, meltwater flushing, and layer combination/division (Flanner et al., 2007; Flanner et al., 2012; Oleson et al., 2010). Therefore, more precipitation and more snow coverage in winter can be a primary factor causing the underestimation of annual mean LAP concentration and LAP-induced snow darkening. Secondly, the associated overestimation in simulated SGS during winter (Figure 4E) can also contribute to the lower $\Delta\alpha$ values simulated in WRF-HR because bigger snow grains in WRF-HR lead to lower clean albedo and thus smaller percentage reduction in albedo compared to STC-MODDRFS. Moreover, we have assumed spherical shaped snow grains in our simulations. Recently, microscopic level studies show that uncertainties associated with simplified snow grain shape treatment in model parameterization can solely contribute to large biases in SNICAR- $\Delta\alpha$ estimates and thus the LAP-snow albedo radiative and snow melt feedback processes (Liou et al., 2014; Dang et al., 2016; He et al., 2017). Thirdly, the fact that the persistent cloud cover over HMA during winter season can induces a lot of uncertainty in the STC-MODSCAG and STC-MODDRFS estimates, is also equally important.

At the same time, uncertainties regarding aerosol emission, transport and deposition to the snow layers are also significant. It is well known that the transport and deposition of black carbon from Indian landmass to Himalayas increases in the afternoon with the evolution of boundary layer over the IGP region (Dumka et al., 2015; Raatikainen et al., 2014). This feature is well simulated by the model (not shown). As STC-MODDRFS estimates are representative of 1000 LT, but simulated values are sampled in the midday (1000-1400 LT), positive biases in aerosol transport and deposition in snow packs (i.e. higher $\Delta\alpha$ values) might be simulated in WRF-HR runs, especially during pre-monsoon months. At the same time, GOCART dust emission parameterization (used here) is dependent on near surface wind speed. Previous studies have evaluated and illustrated inherent uncertainties in dust emission by this parameterization, mostly underestimation over Indian region (Dipu et al., 2013; Kumar et al., 2014). Thus, the uncertainty in local dust emission fluxes over HMA can also contribute to the biases in simulated $\Delta\alpha$ values. Also, large biases in LAP values may be simulated due to model

uncertainties in enhanced wet scavenging fluxes in winter. An overestimation in LAP concentration can lead to an overestimation of snow darkening and melting, resulting in an underestimation of NSD (Figure S4). The large biases in $\Delta\alpha$ values ($> 20\%$) simulated by WRF-HR towards late spring could be attributed to both, underestimation in fSCA and overestimation of LAP concentration in the model.

Although a better quantification of these model biases requires evaluation against in-situ measurements, it is worth mentioning here that no in-situ measurements are available for a direct comparison of these high $\Delta\alpha$ values WRF-HR over W. Himalayas (Gertler et al., 2016). Nonetheless, the high values simulated during pre-monsoon are close to previously reported values over other HMA regions. Kaspari et al., (2014) used the offline SNICAR model to report that BC concentrations in pre-monsoon snow/ice samples at Mera Glacier were large enough to reduce albedo by 6-10% and the reduction in albedo was 40-42% relative to clean snow when dust is included in the calculation. Recently, Zhang et al. (2018) has combined a large dataset of LAP measurements in surface snow with the offline SNICAR model to illustrate that $\Delta\alpha$ can be $>35\%$ over Tibetan Plateau. Moreover, the composite effect of this discrepancy on seasonal/annual mean values is minimal as the snowpack is at its minimum near the end of pre-monsoon season. Similar high daily variability, huge radiative forcing values (LAPRF $\sim 200\text{ W/m}^2$) and sudden decline in snow depth in late pre-monsoon is also reported over upper Colorado river basin (Skiles et al., 2015; Skiles and Painter, 2017).

Impact of light-absorbing particles on snow albedo darkening and associated radiative forcing over High Mountain Asia: High resolution WRF-Chem modeling and new satellite observations

Chandan Sarangi¹, Yun Qian^{1*}, Karl Rittger², Kat J. Bormann³, Ying Liu¹, Hailong Wang¹, Hui Wan¹, Guangxing Lin¹, and Thomas H Painter³

¹Pacific Northwest National Laboratory, Richland, WA

²Institute of Arctic and Alpine Research, Boulder, CO

³Jet Propulsion Laboratory, California Institute of Technology, Pasadena, CA

Submitted to the Atmospheric Chemistry and Physics

September 13, 2018

Corresponding Author: yun.qian@pnnl.gov

Abstract

Light-absorbing particles (LAPs), mainly dust and black carbon, can significantly impact snowmelt and regional water availability over High Mountain Asia (HMA). In this study, for the first time, online aerosol-snow interactions enabled and a fully coupled chemistry Weather Research and Forecasting (WRF-Chem) regional model is used to simulate LAP-induced radiative forcing on snow surfaces in HMA at relatively high spatial resolution (12 km, WRF-HR) than previous studies. Simulated macro- and micro-physical properties of the snowpack and LAP-induced snow darkening are evaluated against new spatially and temporally complete datasets of snow covered area, grain size, and impurities-induced albedo reduction over HMA. A WRF-Chem quasi-global simulation with the same configuration as WRF-HR but a coarser spatial resolution (1 degree, WRF-CR) is also used to illustrate the impact of spatial resolution on simulations of snow properties and aerosol distribution over HMA. Due to a more realistic representation of terrain slopes over HMA, the higher resolution model (WRF-HR) shows significantly better performance in simulating snow area cover, duration of snow cover, snow albedo and snow grain size over HMA, as well as an evidently better atmospheric aerosol loading and mean LAPs concentration in snow. However, the differences in albedo reduction from model and satellite retrievals is large during winter due to associated overestimation in simulated snow fraction. It is noteworthy that Himalayan snow cover have high magnitudes of LAP-induced snow albedo reduction (4-8 %) in pre-monsoon (both from WRF-HR and satellite estimates), which, induces a snow-mediated radiative forcing of $\sim 30\text{-}50 \text{ W/m}^2$. As a result, Himalayas (specifically western Himalayas) hold the most vulnerable glaciers and mountain snowpack to the LAP-induced snow darkening effect within HMA. In summary, coarse spatial resolution and absence of snow-aerosol interactions over Himalaya cryosphere will result in significant underestimation of aerosol effect on snow melting and regional hydroclimate.

1 **1. Introduction**

2 Light-absorbing aerosol particles (LAPs; airborne dust and black carbon (BC) specks), can
3 impact on regional water availability over Asia in three ways. Firstly, LAPs can directly interact
4 with incoming solar radiation and induce thermo-dynamical modifications to synoptic scale
5 circulations (Hansen et al., 1997 ; Ramanathan et al., 2001; Bond et al., 2013; Lau et al., 2006;
6 Bollasina et al., 2011; Li et al., 2016). Secondly, acting as cloud condensation nuclei, changes in
7 concentrations of these particles can lead to microphysical modification of cloud systems and
8 precipitations (Fan et al., 2016; Li et al., 2016 ; Qian et al., 2009; Sarangi et al., 2017). Finally,
9 deposition of LAPs in the snowpack can also darken the snow, reduce its surface albedo and
10 accelerate snow warming and melting (Warren and Wiscombe, 1980; Qian et al., 2015; Qian et
11 al., 2011; Qian et al., 2009a; Lau et al., 2010; Xu et al., 2009; Hadley and Kirchstetter, 2012;
12 Dang et al., 2017). Modeling studies have suggested that the LAP-induced snow darkening
13 mechanism has warming and snow-melting efficacy even greater than that of greenhouse gases
14 (GHGs) (Hansen and Nazarenko, 2004; Flanner et al., 2007; Qian et al., 2011; Skiles et al., 2012).
15 To give a perspective, the concentration of just 100 ng of BC in 1 g of snowpack will reduce the
16 visible-wavelength albedo of grain radius 1000 μm by 10% (Fig. 1b of Warren, 2013). A chain of
17 positive feedback mechanisms results in such large impact of LAPs (Qian et al., 2015). Initially,
18 as snow starts to melt, the concentration of LAPs in snowpack increases because a portion of
19 LAPs accumulate at the surface of the snowpack instead of getting washed away with
20 meltwater (Conway et al., 1996; Flanner et al., 2007; Doherty et al., 2010). This increase in LAP
21 concentration leads to enhanced warming of the snowpack and thereby increases the effective
22 snow grain size, which further lowers snow albedo (Warren and Wiscombe, 1980; Hadley and

23 Kirchstetter, 2012). Nonetheless, at higher concentrations, grain sizes can again be reduced due
24 to the loss of mass from surface layers with the intense melting (Painter et al., 2013). As this
25 process continues, sufficient snow melt occurs to expose the darker underlying surface, leading
26 to enhanced warming and snow ablation commonly-known as “snow albedo feedback”
27 (Warren and Wiscombe, 1980; Hansen and Nazarenko, 2004; Flanner et al., 2007; Qian et al.,
28 2015). In turn, this earlier loss of snow cover induces surface warming and perturbing regional
29 circulations (Hansen and Nazarenko, 2004; Lau et al., 2010; Qian et al., 2011). This LAP-induced
30 modification of snow albedo feedback is identified as one of major forcing agents affecting
31 climate change with a high level of uncertainty (IPCC, 2013).

32 High Mountain Asia (HMA) includes the Tibetan plateau, central Asian mountains and
33 the Himalaya cryosphere. It holds the largest glacial cover (~9500 glaciers) outside the polar
34 region (Dyrgerov, 2001). Observations revealed that a historical decadal increase in the
35 surface air temperature over HMA in a range of 0.6-1.8 °C (Shrestha et al., 1999; Wang et al.,
36 2008), and the warming is faster over higher elevations (> 4000 m) in the last three decades (Xu
37 et al., 2009b; Ghatak et al., 2014). The Himalaya glacier area has cumulatively decreased by
38 ~16% during the period 1962 to 2004 (Kulkarni et al., 2010) and the pre-monsoon snow cover is
39 decreasing at a decadal rate of ~0.8 million km² during the last 50 years (Brown and Robinson,
40 2011). The average retreat rate on the north slope of Mount Everest is as high as 5.5–9.5 m y⁻¹
41 (Ren et al., 2006). The Himalaya cryosphere contributes to the stream flow in Indus and Ganges
42 river systems by ~ 50 % and ~10-30%, respectively (Khan et al., 2017). Warming and glacier
43 retreat over the Himalaya cryosphere have a great potential to impact the fresh water
44 availability for about 700 million people, modify regional hydrology, and disturb the agrarian

45 economy of all South Asian countries (Bolch et al., 2012; Immerzeel et al., 2010; Kaser et al.,
46 2010; Singh and Bengtsson, 2004; Barnett et al., 2005; Yao et al., 2007). Therefore, it is critical to
47 disentangle the factors contributing to glacier retreat and snow melt over HMA.

48 Regional warming due to increasing greenhouse gases (Ren and Karoly, 2006) has been
49 reported as the primary cause of the high rate of warming and glacier retreat over HMA.

50 However, in the last decade, advancement in remote sensing and availability of measurements
51 from several field campaigns suggest that the contribution of LAP loading (in the atmosphere)
52 to the warming and glacier melting over HMA is probably greater than previously believed
53 (Ramanathan et al., 2007; Prasad et al., 2009; Menon et al., 2010). Continuous observations
54 over the Nepal Climate Observatory Pyramid (NCO-P) facility located at 5079 m a.s.l. in the
55 southern foothills of Mt. Everest revealed very high concentrations of black carbon (Marcq et
56 al., 2010) and desert dust (Bonasoni et al., 2010) especially in pre-monsoon from Indo-Gangetic
57 plains. Atmospheric LAPs are scavenged to the snow/ice surface by dry and wet deposition and
58 cause measurable snow darkening and melting (Gautam et al., 2013; Yasunari et al.,
59 2010b; Yasunari et al., 2013; Nair et al., 2013; Ménégoz et al., 2014; Ming et al., 2008; Flanner
60 and Zender, 2005). Thus, LAP deposited in snow and associated snow darkening has been
61 suggested as a key factor to the early snowmelt and rapid glacier retreat over HMA (Yasunari et
62 al., 2010; Ming et al., 2008; Xu et al., 2009a; Flanner et al., 2007; Qian et al., 2011).

63 While previous studies have underlined the significance of LAP-deposition in snow over HMA,
64 the estimation of LAP-induced snow darkening and associated radiative forcing is still highly
65 uncertain (Qian et al., 2015). **Many of these studies used online global model simulations at**
66 **coarse spatial resolutions of ~50-150 km (Flanner and Zender, 2005; Ming et al., 2008; Qian et**

67 al., 2011; Kopacz et al., 2011; Zhang et al., 2015). Other studies employed offline simulation of
68 the snow albedo effect using measured or modelled concentrations of deposited LAP in surface
69 snow or estimated from atmospheric loading and ice cores (Yasunari et al., 2013; Nair et al.,
70 2013; Wang et al., 2015; He et al., 2014; Santra et al., 2019; Thind et al., 2019). The complex
71 terrain of HMA, seasonal snowfall and near surface air circulation are not well resolved by
72 coarse global climate models (Kopacz et al., 2011; Ménégoz et al., 2014). Similarly, offline
73 estimations are limited in scope because they are site specific and are based on simplified
74 assumptions about deposition rates. Ideally, online high resolution simulations allowing for
75 LAP-snow interactions should facilitate a more realistic understanding of LAP deposition to
76 snow and LAP-induced snow darkening effect in terms of both magnitude and spatial variability
77 over HMA.

78 In this study, a modified version of the online chemistry coupled with Weather Research
79 and Forecasting regional model (WRF-Chem v3.5.1), which, is then fully coupled with SNICAR
80 (SNow, ICe, and Aerosol Radiative) model, is used to perform first-ever high resolution (12 km)
81 simulation over the HMA region for the water year 2013-14 (October 1, 2013 to September 30,
82 2014). Satellite observations of snow properties like snow albedo, grain size, and LAP-induced
83 snow darkening from MODSCAG and MODDRFS retrievals are used for evaluation (Painter et al,
84 2009; 2012). The main objective of this study is to evaluate the skill of high resolution WRF-
85 Chem model in simulating properties of snowpack, aerosol distribution, LAP in snow and LAP-
86 induced snow darkening over HMA using spatially and temporally complete (STC) remotely
87 sensed snow surface properties (SSP) from MODIS (Dozier et al, 2008; Rittger et al, 2016). Our
88 second objective is to demonstrate the benefit for aerosol and snow distributions in high

89 resolution runs by comparing to a coarse gridded quasi-global model simulation over HMA. This
90 quasi-global simulation is run with the same WRF-Chem configuration but at 1 degree spatial
91 resolution. Finally, the spatiotemporal variation of simulated LAP deposition, snow albedo
92 darkening and snow mediated LAP radiative forcing (LAPRF) over HMA are discussed. The
93 model details and datasets used are described in Section 2. Results and discussions are
94 presented in Section 3 followed by conclusions in Section 4.

95 **2: Model simulations and observational datasets**

96 Below, we provide details on the aerosol module used in WRF-Chem, interactive
97 coupling with aerosol and SNICAR via land model, and the model setup for both 12 km and 1
98 degree resolution runs. The details for the remote sensing observations that are used to
99 evaluate the models are also provided.

100 **2.1: Coupled WRF-Chem-CLM-SNICAR Model description**

101 The WRF-Chem simulation is performed at 12 km × 12 km horizontal resolution
102 (hereafter refereed as WRF-HR) with 210 × 150 grid cells (64–89°E, 23–40°N) (Figure 1) and 35
103 vertical layers. The simulation was conducted from 20th September, 2013 to 30th September,
104 2014, to provide one year of results (following a 10-day model spin-up). ERA-interim reanalysis
105 data at 0.7° horizontal resolution and 6 h temporal intervals are used for meteorological initial
106 and lateral boundary conditions. The simulation is re-initialized every 4th day to prevent the
107 drift of model meteorology. Model physics options used are the MYJ (Mellor–Yamada– Janjic)
108 planetary boundary layer scheme, Morrison 2-moment microphysics scheme, community land

109 model (CLM), Kain-Fritsch cumulus scheme and Rapid Radiative Transfer Model for GCMs
110 (RRTMG) for longwave and shortwave radiation schemes.

111 The CBM-Z (carbon bond mechanism) photochemical mechanism (Zaveri and Peters,
112 1999) coupled with eight bin MOSAIC (Model for Simulating Aerosol Interactions and
113 Chemistry) aerosol model (Zaveri et al., 2008) is used. This is the most sophisticated aerosol
114 module available for the WRF-Chem model. The sectional approach with eight discrete size bins
115 is used to represent the size distributions of all the major aerosol components (including
116 sulfate, nitrate, ammonium, black carbon (BC), organic carbon (OC), sea salt, and mineral dust)
117 in the model. The processes of nucleation, condensation, coagulation, aqueous phase
118 chemistry, and water uptake by aerosols in each bin size are included in the MOSAIC module.
119 Dry deposition of aerosol mass and number is simulated by including both diffusion and
120 gravitational effects as per Binkowski and Shankar (1995). Wet removal of aerosols follow
121 Easter et al. (2004) and Chapman et al. (2009) and includes grid resolved impaction and
122 interception processes for both in-cloud (rainout) and below-cloud (washout) aerosol removal.
123 Processes involved in convective transport and wet removal of aerosols by cumulus clouds are
124 described in Zhao et al. (2013).

125 Anthropogenic emissions used in our study is at $0.5^\circ \times 0.5^\circ$ horizontal resolution and are
126 taken from the NASA INTEX-B mission Asian emission inventory for year 2006 (Zhang et al.,
127 2009). Biomass burning emissions at $0.5^\circ \times 0.5^\circ$ horizontal resolution for the water year 2013-
128 14 are obtained from the Global Fire Emissions Database, Version 3 (GFEDv3) (Van Der Werf et
129 al., 2010), which are vertically distributed in our simulation using the injection heights
130 prescribed by Dentener et al. (2006) for the Aerosol Inter Comparison project (AeroCom). Sea

131 salt and dust emissions follow Zhao et al. (2014). Dust surface emission fluxes are calculated
132 with the Georgia Institute of Technology-Goddard Global Ozone Chemistry Aerosol Radiation
133 and Transport (GOCART) dust emission scheme (Ginoux et al., 2001), and emitted into the eight
134 MOSAIC size bins with respective mass fractions of 10^{-6} , 10^{-4} , 0.02, 0.2, 1.5, 6, 26, and 45%.

135 Aerosol optical properties are computed as a function of wavelength for each model
136 grid cell. The Optical Properties of Aerosols and Clouds (OPAC) data set (Hess et al., 1998) is
137 used for the shortwave (SW) and longwave (LW) refractive indices of aerosols and a complex
138 refractive index of aerosols (assuming internal mixture) is calculated by volume averaging for
139 each chemical constituent of aerosols for each bin. A spectrally-invariant value of $1.53 \pm 0.003i$
140 is used for the SW complex refractive index of dust. Fast et al. (2006) and Barnard et al. (2010)
141 provide detailed descriptions of the computation of aerosol optical properties such as
142 extinction coefficient, single scattering albedo (SSA), and asymmetry factor in WRF-Chem.
143 Following Zhao et al. (2011) and Zhao et al. (2013a), aerosol radiative feedback is coupled with
144 the Rapid Radiative Transfer Model (RRTMG) (Mlawer et al., 1997) and the direct radiative
145 forcing of individual aerosol species in the atmosphere are diagnosed. Aerosol–cloud
146 interactions are included in the model following Gustafson et al. (2007).

147 The increasingly used Snow, Ice, and Aerosol Radiation (SNICAR) model simulates the snow
148 properties and associated radiative heating rates of multilayer snow packs (Flanner and Zender,
149 2005; Flanner et al., 2009, 2012 and 2007). Fundamentally, it employs the snow albedo theory
150 (parameterization) based on Warren and Wiscombe (1980) and the two-stream radiative
151 approximation for multilayers from Toon et al. (1989). SNICAR can also simulate aerosol
152 radiative effect in snow for studying the LAP heating and snow aging (Flanner et al., 2007).

153 Recently, laboratory and site measurements are used to validate the SNICAR simulated change
154 of snow albedo for a given BC concentration in snow (Hadley and Kirchstetter, 2012; Brandt et
155 al., 2011). For radiative transfer calculations, SNICAR defines layers matching with the five
156 thermal layers in community land model (CLM) that vertically resolve the snow densification
157 and meltwater transport (Oleson et al., 2010). **Note that the number of snow layers and**
158 **thickness of top snow surface layer are predicted in the CLM model. Fresh snowfall and melting**
159 **continuously affect the model surface snow layer thickness (3 cm or less). Therefore, LAP**
160 **concentrations within each snow layer depend on meltwater flushing, new snowfall and**
161 **associated top layer evolution (Flanner et al., 2007, 2012; Oleson et al., 2010).** In WRF-Chem-
162 SNICAR coupled model, BC and dust deposition on snow is calculated in a prognostic approach
163 through dry and wet deposition processes. BC in snow can be represented as externally and
164 internally mixed with precipitation hydrometeors depending on the removal mechanism
165 involved, but dust is considered to only mix externally with snow grains (following Flanner et
166 al., 2012). SNICAR in WRF-Chem simulates four tracers of dust based on size (with diameters of
167 0.1–1, 1–2.5, 2.5–5, and 5–10 μm) and two tracers of BC (externally and internally mixed BC
168 with 0.2 μm dry diameter) in snow. The MOSAIC aerosol model simulates dust in the
169 atmosphere with eight size bins (0.039–0.078, 0.078–0.156, 0.156–0.312, 0.312–0.625, 0.625 -
170 1.25, 1.25–2.5, 2.5–5.0, and 5.0–10.0 μm in dry diameter). The first 4 bins are coupled with the
171 smallest bin of dust particles in SNICAR. While the next two MOSAIC bins (5th and 6th) map into
172 the second bin of SNICAR, the 7th and 8th MOSAIC dust bins correspond to the third and fourth
173 SNICAR dust bins (Zhao et al., 2014), respectively. Deposition of LAPs to snow in SNICAR are
174 immediately mixed in the CLM surface snow layer (< 3 cm). CLM adds excess water in the layer

175 above to the layer beneath during melting. The scavenging of aerosols in snow by meltwater is
176 assumed to be proportional to its mass mixing ratio of the meltwater multiplied by a scavenging
177 factor. Scavenging factors for externally mixed BC and internally mixed BC are assumed to be
178 0.03 and 0.2, respectively, and 0.02, 0.02, 0.01, and 0.01 for the four dust bins (all externally
179 mixed). Although these scavenging factors are comparable to observations (Doherty et al.,
180 2013), the scavenging ratios can be highly heterogeneous and introduce high uncertainty into
181 the estimation of LAP concentrations in snow (Flanner et al., 2012; Qian et al., 2014). More
182 detailed description about the aerosol deposition and mixing processes, computation of optical
183 properties of snow and LAPs in WRF-Chem-CLM-SNICAR coupling can be found in Zhao et
184 al.(2014) and Flanner et al.(2012).

185 Configured in the way similar to the WRF-HR, a coarse ($1^\circ \times 1^\circ$) gridded WRF-Chem
186 simulation is also performed using a quasi-global model (hereafter referred as WRF-CR) with
187 360×130 grid cells (180° W– 180° E, 60° S– 70° N). Periodic boundary conditions are used in the
188 zonal direction. Reanalysis of the TROpospheric (RETRO) anthropogenic emissions for the year
189 2010 ([ftp://ftp.retro.enes.org/ pub/emissions/aggregated/anthro/0.5x0.5/](ftp://ftp.retro.enes.org/pub/emissions/aggregated/anthro/0.5x0.5/)) is used for
190 anthropogenic aerosol and precursor gas emissions in the coarse gridded quasi-global WRF-
191 Chem simulation except for Asia and the United States. INTEX-B anthropogenic emissions
192 (Zhang et al., 2009) and US National Emission Inventory are used for Asia and the U.S.,
193 respectively. Emissions of biomass burning aerosols, sea salt, and dust are treated in the same
194 way as described above for the WRF-HR simulation. More details about the quasi-global WRF-
195 Chem simulation can be found in (Zhao et al., 2013b);Hu et al., 2016). Chemical initial and

196 boundary conditions to the WRF-HR simulation are provided by this quasi-global WRF-CR runs
197 for the same time period to include long-range transported chemical species.

198 **2.2: Aerosol Optical Depth (AOD) dataset**

199 The aerosol robotic network (AERONET – <https://aeronet.gsfc.nasa.gov>) is a global
200 network of ground based remote sensing stations that provides quality-controlled
201 measurements of AOD with uncertainties ~ 0.01 under clearsky conditions over India (Holben et
202 al., 1998; Dubovik et al., 2000). CIMEL Sun scanning spectral radiometers are used to measure
203 direct Sun radiance at eight spectral channels (340, 380, 440, 500, 675, 870, 940, and 1020 nm)
204 and measure spectral columnar AOD (Holben et al., 1998). AERONET provides measurements at
205 ~ 15 min temporal resolution from sunrise to sunset.

206 Skyradiometer Network (Skynet) is another global network of ground based spectral
207 scanning radiometer (POM-01L, Prede, Japan) stations that provides quality-controlled
208 measurements of AOD (Nakajima et al., 1996). With an automatic sun scanner and sensor, it
209 measures sky irradiance in five wavelengths i.e. 400, 500, 675, 870, and 1020 nm. The
210 measured monochromatic irradiance data is processed by using Skyrad.Pack version 4.2
211 software. Calibration of the Sky radiometer is carried out on a monthly basis
212 (<http://atmos3.cr.chiba-u.jp/skynet/data.html>). Details of the instrumentation and software
213 protocol can be found in Campanelli et al. (2007) and Ningombam et al., (2015). In this study,
214 we have also used AOD measurements at 500 nm over MERAK, a high altitude Skynet station in
215 Himalaya for water year 2013-14.

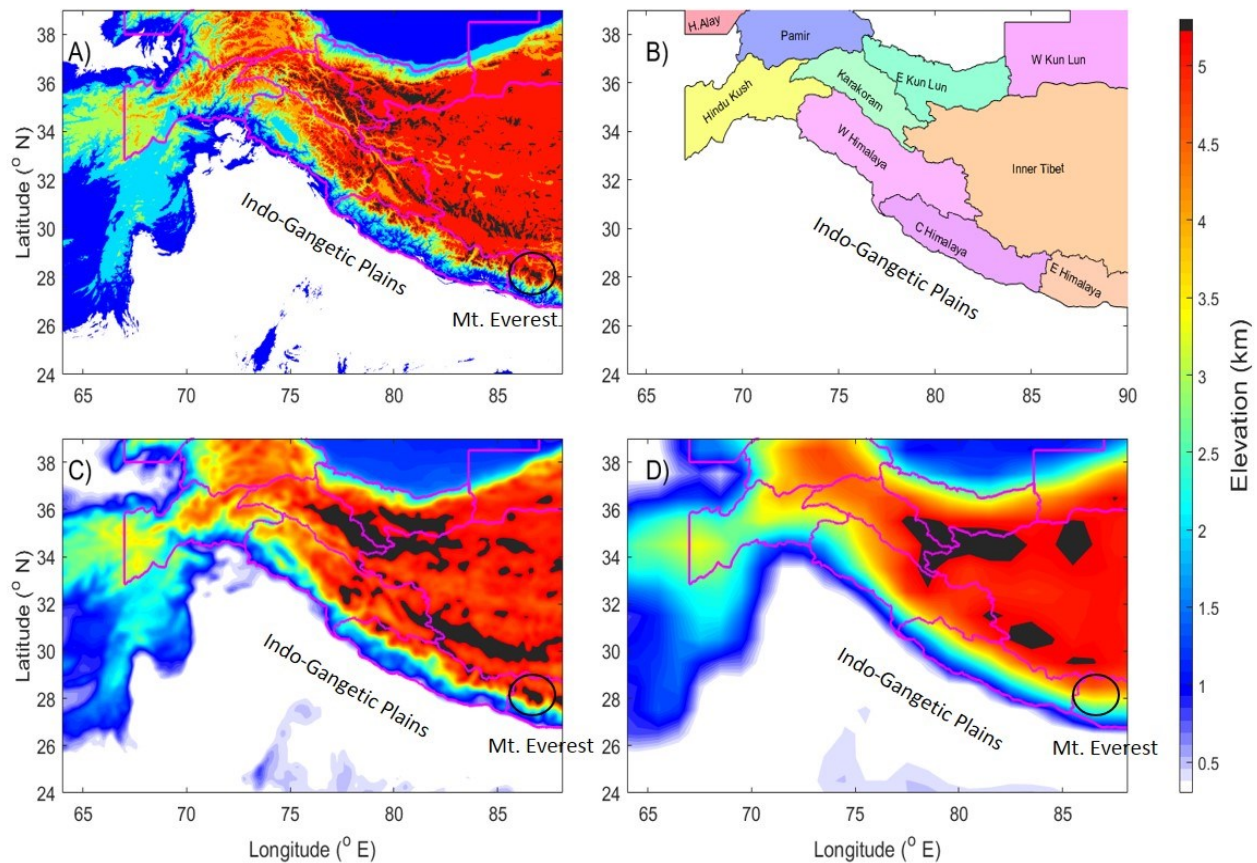
216 The MODerate resolution Imaging SpectroRadiometer (MODIS) instrument onboard the
217 NASA AQUA satellite provides global coverage of daily radiance observations (at 1330 LT) in 36
218 spectral channels. Over North India, Tripathi et al., (2005) has shown that MODIS observations
219 correlate well with ground based measurements. For the evaluation of model simulated AOD,
220 1° gridded Level 3 AOD estimates (collection 6) at 0.55 μm wavelength obtained from the
221 MODIS instrument are used during water year 2013-14. However, the MODIS land aerosol
222 algorithm uses a dark target approach (Levy et al., 2007), which, is known to have large
223 uncertainties over arid and mountainous surfaces (Levy et al., 2010).

224 **2.3: Spatially and temporally complete MODSCAG and MODDRFS retrievals**

225 Subpixel snow-covered area and snow grain size are retrieved from MODIS-observed
226 surface reflectance data using the physically based MODIS Snow-Covered Area and Grain size
227 (MODSCAG) (Painter et al., 2009) algorithm. In each snow covered pixel, MODSCAG attributes a
228 fractional snow-covered area and grain size using spectral mixture analysis to determine
229 proportion of the pixel that is snow and is not snow. MODSCAG is more accurately identifies
230 snow cover throughout the year than the widely used MODIS snow product: MOD10A1 (Rittger
231 et al., 2013). The MODSCAG snow-mapping algorithm for fraction of snow covered area has an
232 uncertainty of $\sim 5\%$ (Rittger et al., 2013). The current study incorporates pixel level snow cover
233 area and snow grain size from MODSCAG over the HMA region to evaluate snow pack
234 simulation and LAP-induced albedo reduction. Further, MODIS Dust Radiative Forcing in Snow
235 (MODDRFS) model (Painter et al., 2012) is used to determine the LAP-induced albedo reduction
236 over HMA. MODDRFS uses spectral reflectance differences between the measured snow
237 spectral albedo and the modeled clean snow spectral albedo. The pixel level clean snow

238 spectrum corresponding to MODSCAG retrieved snow grain sizes is calculated using discrete
239 ordinate radiative transfer solutions for visible wavelengths and solar zenith angles. Coupled,
240 these products provide the determination of snow albedo for the fractional snow cover with
241 LAP inclusion.

242 Reflectance inputs to MODSCAG and MODDRFS are degraded by cloud cover, off-nadir
243 views, and data errors, but can be filtered in time and space to improve data quality and
244 consistency. Our method for spatially cleaning and filling (Dozier et al., 2008;Rittger et al., 2016)
245 combines noise filtering, snow/cloud interpolation and smoothing to improve the daily
246 estimates snow surface properties (SSP). Using remotely sensed forest height maps (Simard et
247 al., 2011) and MODSCAG vegetation fraction, we adjust the satellite viewable snow cover to
248 account for snow under tree canopy (Rittger et al., 2016). We weight the observations based
249 on satellite viewing angle that varies from 0 to 65 degree with larger uncertainties in off-nadir
250 views (Dozier et al., 2008). The result is a set of spatially and temporally complete (STC) SSPs.
251 Use of these products in an energy balance model to estimate snow water equivalent based on
252 reconstruction produced more accurate snow cover than the Snow Data Assimilation System
253 (SNODAS) or an interpolation of observations from snow pillows (Bair et al., 2016). In this study
254 we use STC versions of MODSCAG and MODDRFS when comparing our WRF model output. The
255 incomplete remotely sensed would be difficult to use given the gaps in data and uncertainties
256 related to viewing angle (Dozier et al., 2008). Hereafter, the use of MODSCAG and MODDRFS
257 terms will invariably refer to these STC-MODSCAG and STC-MODDRFS products.



258
 259 Figure 1: Panel A illustrates the terrain elevation at 1 km resolution from ETOPO1 dataset. Panel
 260 B shows glacier classification over HMA region used in this study following Randolph Glacier
 261 Inventory. Panels C and D illustrate terrain representation in WRF-HR run (12 km) and WRF-CR
 262 (1 degree) runs, respectively. For reference, Mt. Everest (shown as black circle in Figure 1C) is
 263 distinctly represented in Panel A and C, but not in Panel B.

264

265 **2.4: Variation in terrain representation in WRF-HR and WRF-CR**

266 Figure 1A illustrates the variations in terrain height over HMA at a resolution of 1 arc
 267 using ETOPO1 Global Relief Model, a publicly available global topographical dataset (Amante
 268 and Eakins, 2009). It clearly shows the enormous relief in terrain as we move from the Indo
 269 Gangetic plains (IGP) to the crest of the Himalaya and into the Tibetan Plateau (TP). The
 270 majority of HMA is above 4 km altitude with many Himalaya peaks at an altitude higher than 6

271 km. Figure 1B illustrates the mountain ranges and glaciers classified as per the Randolph Glacier
272 Inventory in the Fifth Assessment Report of the Intergovernmental Panel on Climate Change
273 (Pfeffer et al., 2014). Specifically, Pamirs, Hindu Kush, Karakoram, Kunlun, and Himalaya hold
274 the most number of glaciers in HMA. Figures 1C and 1D illustrate the representation of terrain
275 elevation in WRF-HR and WRF-CR, respectively. Compared to Figure 1A, location of mountain
276 peaks (altitude > 5.5 km) are better represented in WRF-HR compared to WRF-CR, as is
277 particularly evident over the Karakoram, Kunlun, and Himalaya ranges. Moreover, the steep rise
278 in elevation between IGP and TP is also well represented by WRF-HR, whereas it is more
279 gradual in WRF-CR.

280 **2.5: Methodology**

281 Simulation of the snow macro- and micro-physical properties, aerosol loading and LAP in
282 snow concentration from WRF-HR, WRF-CR and observational estimates (datasets described
283 above) over HMA are compared in Section 3.1 and Section 3.2. In Section 3.3, the WRF-HR
284 simulated LAP-induced snow albedo reduction values over HMA is compared with
285 corresponding MODIS satellite based STC-MODSCAG and STC-MODDRFS. Lastly, a discussion on
286 the high resolution model simulated LAP-induced radiative forcing estimates over HMA is also
287 presented in context to previous studies and other atmospheric forcing.

288 The simulated fractional snow covered area (fSCA), duration of snow cover over a grid in
289 terms of number of snow cover days (NSD), snow albedo (α) and snow grain sizes (SGS) and
290 LAP-induced snow albedo darkening ($\Delta\alpha$) for midday (1000 -1400 LT) conditions from both the
291 WRF models are compared with corresponding STC-MODSCAG and STC-MODDRFS retrievals

292 over HMA. The number of snow cover days (NSD: defined as days having fSCA values ≥ 0.01)
293 during water year 2013-14 is determined over each grid from STC-MODSCAG and both model
294 runs. They are compared with corresponding values from STC-MODSCAG retrievals, which, are
295 observed during Terra overpasses at 10:30 LT. We have used a window from 10:00 LT to 14:00
296 LT for representing midday averages of modelled variables to incorporate the variability due to
297 differences in timing (between model and real scenario) of weather conditions like precipitation
298 and clouds. In addition, the change in snow albedo during 10:00 - 14:00 LT is < 0.01 (Bair et al.,
299 2017), which, is low compared to other model physics- and data retrieval related uncertainties.
300 The WRF-CR simulated variables and STC-MODSCAG and STC-MODDRFS retrievals are gridded
301 to the resolution of WRF-HR (12 km) for ease of comparison. We have compared annual mean
302 values as well as seasonal mean values for winter (December - February) and pre-monsoon
303 (April - June) season, separately. We have not considered the monsoon period in our analyses
304 because the snow cover during the monsoon is negligible (except in glaciated regions at high
305 altitudes) relative to other months (Figure S1). **Simulated SGS values only from the topmost**
306 **snow surface layer is compared to the MODSCAG SGS retrievals.** To evaluate spatial
307 heterogeneity in our model, the seasonal and annual distribution of these variables are
308 calculated separately for each sub region (shown in Figure 1) within HMA. In addition, to gain
309 an understanding of the extent of temporal variability present in LAP-induced effects, we have
310 also presented daily midday variation in LAP-induced snow darkening and LAP-induced
311 radiative forcing at surface over Chotta Shingri glacier region (32.1-32.35 °N, 77.4-77.7 °E)
312 located in the Chandra–Bhaga river basin of Lahaul valley, Pir Panjal range, in Western
313 Himalayas. It is an accessible and representative site for glacier mass balance studies in western

314 Himalayas. Chotta Shigri glacier has a cumulative glaciological mass loss of -6.72 m w.e.
315 between 2002 and 2014 (Azam et al., 2016).

316 The simulated aerosol optical depth (AOD) is compared with available in-situ observations
317 (described in Section 2.2). Here, quality assured (Level 2) midday (1000 to 1400 LT) averages of
318 AOD (550 nm) at seven AERONET stations (Lahore, Jaipur, Kanpur, Gandhi college, Kathmandu
319 and CAS) and one SkyNet site within our study region are used to evaluate the simulated AOD
320 values. Further, the simulated distribution of LAP concentration in snow at a few sites is
321 compared with field measurements. Only a few field measurements of concentration of BC
322 (LAP_{BC}) and dust particles (LAP_{dust}) in the snow surface or the surface layer are available over
323 glaciated regions within our study domain. In this study, measurements of LAP_{BC} over Muztagh
324 Ata in eastern slopes of Pamirs (Xu et al., 2006), Uttaranchal region of W. Himalayas (Svensson
325 et al., 2018), East Rongbuk at 6.4 km altitude (Ming et al., 2012; Ming et al., 2008; Xu et al.,
326 2009a) and composite of recent in-situ measurements from various studies near the NCO-
327 pyramid site in Nepal at 5-6 km altitude (Kaspari et al., 2014; Yasunari et al., 2013; Jacobi et al.,
328 2015; Ginot et al., 2014) is used. We have used more than one study to have a range of annual
329 mean LAP values over each location so in principle the observations are representative of
330 different years and different snow depths over the same glacier. Moreover, simulated annual
331 mean LAP concentration only from the topmost snow surface layer is compared to the
332 observed surface snow LAP in snow concentration, which introduce differences in the snow
333 sample depth used for the evaluation. However, to minimize the influence of snow sample
334 depth variation, we have only used data in the literature which are observed as snow surface
335 measurement or from snow pits having a thickness less than 15 cm. Similarly, the point

336 measurements used for evaluating LAP_{dust} are over Abramov glacier in western slopes of Pamirs
337 (Schmale et al., 2017), Muztagh Ata in eastern slopes of Pamirs (Wake et al., 1994) , East
338 Rongbuk (Ming et al., 2012) and near NCO-pyramid station (Ginot et al., 2014), respectively.

339

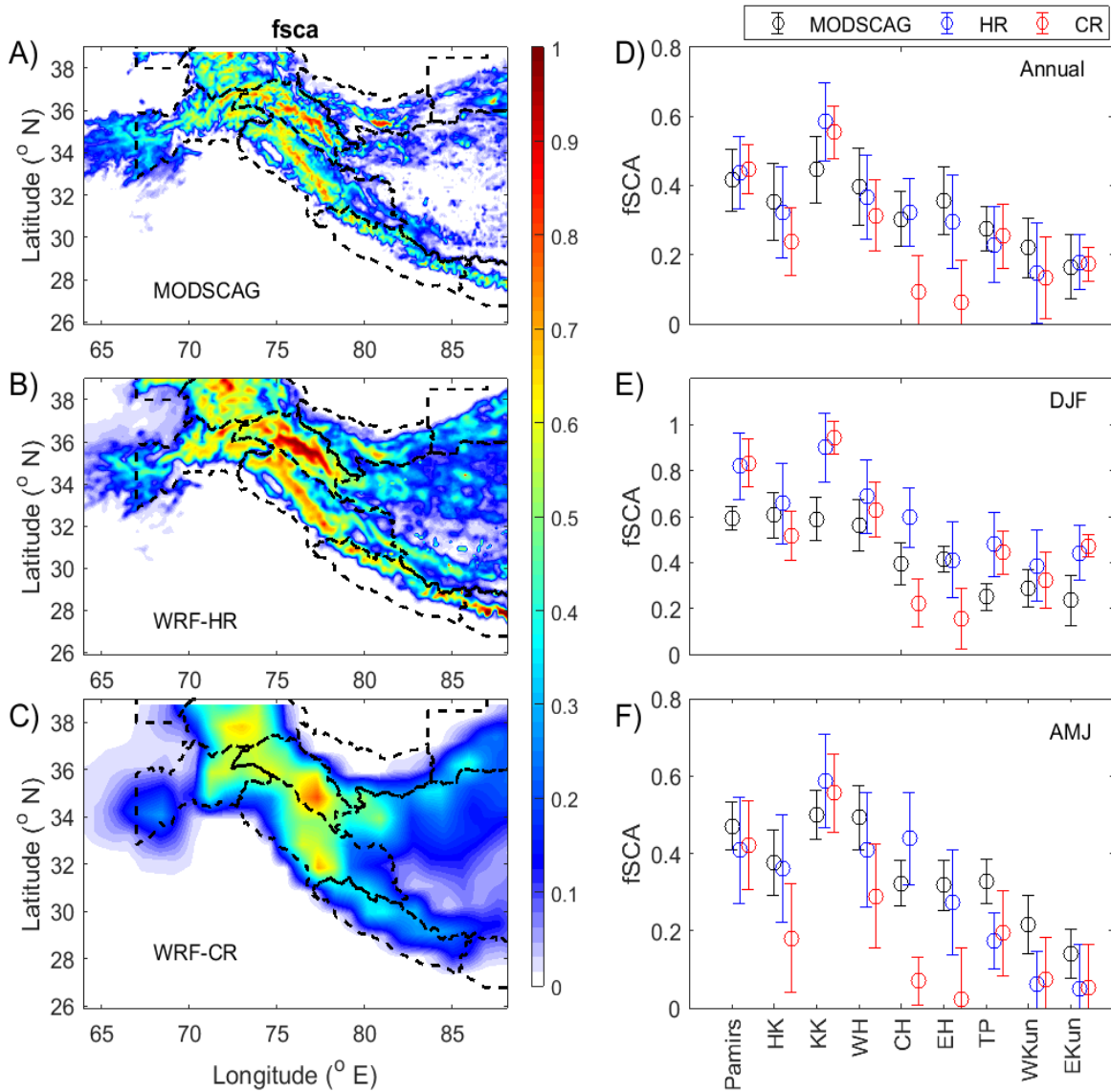
340 **3: Results and Discussions**

341 **3.1: Snow physical, microphysical and optical properties**

342 The largest values of region-averaged annual mean fSCA within HMA are observed in both the
343 satellite retrievals and the model runs over the Karakoram region (mean=0.45) followed by
344 Pamirs, Himalayas and Hindu Kush in the HMA region (Figures 2A and 2B). In comparison, the
345 fSCA over Kunlun and TP are lower (<0.3), but, pockets of very high fSCA (~0.7) are visible over
346 the west Kunlun ranges (Figure 2A). The annual mean fSCA values and the fine spatial variability
347 are well simulated by WRF-HR (Figure 2B) over the entire HMA region. Of exception are
348 simulations over the Karakoram, where WRF-HR overestimates annual mean fSCA, however,
349 the distribution of annual mean fSCA from WRF-HR and STC-MODSCAG agree in all the sub
350 regions (Figure 2D). This observation is largely valid also for pre-monsoon months (Figure 2F).
351 But, significant overestimation in distribution of fSCA (by >0.2) during winter is present over
352 Pamirs, Karakoram, W. Himalayas, TP and Kunlun region (Figures 2E). STC-MODSCAG retrievals
353 illustrate that the Pamirs (NSD=230 days) and Karakoram (NSD=270 days) ranges remain snow
354 covered for 7-9 months of the year (Figure 3A). Similarly, the grids in Hindu Kush (NSD=194), W.
355 Himalayas (NSD=189 days) and C. Himalayas (NSD=191 days) are snow covered for ~ 6-7
356 months. Mountains in E. Himalayas (NSD=142 days) remain snow covered for only 4-5 months

357 of the year. The distribution of annual NSD values simulated by WRF-HR in each sub region is
358 close to STC-MODSCAG values (Figure 3D). Also, the spatial distribution and magnitude of
359 simulated NSD by WRF-HR is similar to that from STC-MODSCAG for different seasons,
360 separately (Figure S2). Thus, overestimation of annual mean fSCA in WRF-HR during winter is
361 not due to mere averaging error associated with underestimation in simulated NSD during
362 winter (Figure S2).

363



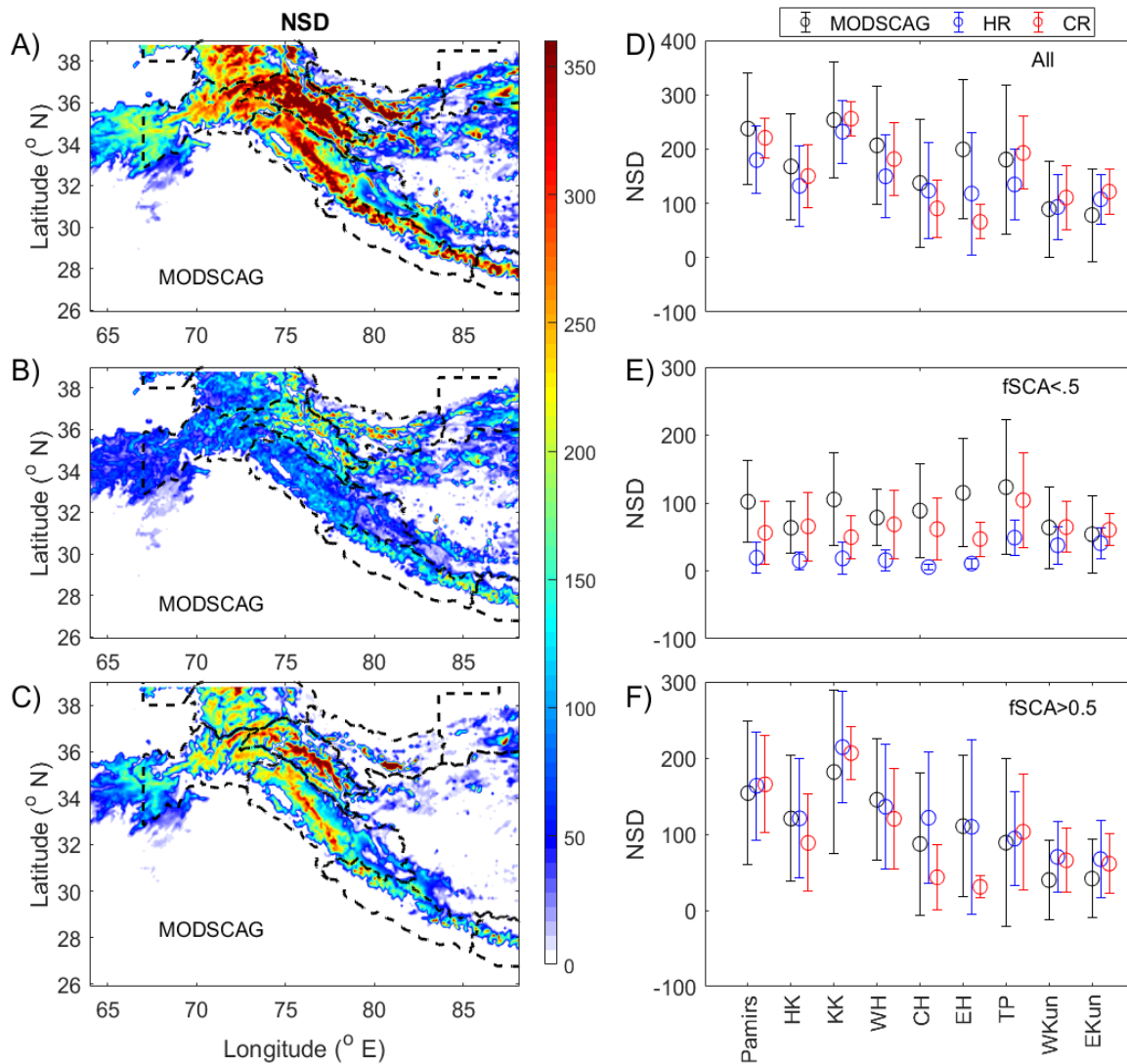
364

365 Figure 2: Spatial distribution of annual mean snow cover fraction (fSCA) during midday (1000-
 366 1400 LT) for water year 2013-14 from A) STC-MODSCAG retrievals, B) simulated values from
 367 WRF-HR and C) WRF-CR simulations. Panels D-F illustrate the distribution of midday mean fSCA
 368 over each subregion identified by glacier classification following Randolph Glacier Inventory (X-
 369 axis). The circle and vertical legs represent mean \pm standard deviation over each region for D)
 370 entire year, E) winter (December - February) and F) pre-monsoon (April - June) season,
 371 separately. Here, Hindu Kush, Karakoram, W.Himalayas, C.Himalayas, E.Himalayas, Tibetan
 372 Plateau, West Kunlun and East Kunlun regions are abbreviated as HK, KK, WH, CH, EH, TP, WKun
 373 and EKun, respectively.

374

375 We also calculated the number of days of snow cover with low fSCA (<0.5; Figure 3B) and high
376 fSCA (>0.5; Figure 3C) values, separately. The grids in Kunlun, Northern slope of Karakoram,
377 eastern slope of Pamirs and TP region are dominated by snow cover of relatively low fSCA for
378 most of their snow cover duration (Figure 3B). But, grids in Hindu Kush, Himalayas and southern
379 slopes of Karakoram are generally covered with high fSCA values throughout the year (Figure
380 3C). The distribution of simulated NSD values over each sub region for low and high fSCA
381 scenario is shown in Figures 3E and 3F, respectively. WRF-HR can well simulate the NSD over
382 grids with high fSCA (Figure 3F) but significantly underestimates NSD over grids with low snow
383 cover (Figure 3E). Note that the regions dominated by low annual fSCA in this water year are
384 actually the same regions where WRF-HR simulated fSCA values are being overestimated in
385 winter (Figure 2E). Thus, simulation of fewer number of days with low fSCA (and vice versa) in
386 WRF-HR might also be contributing partially to the overestimation of winter fSCA simulated in
387 WRF-HR compared to STC-MODSCAG. Further, WRF-HR simulated annual surface rainfall in
388 winter is overestimated over Karakoram, Himalayan and Hindukush ranges (Figure S3). This
389 indicates that overestimation of surface precipitation in WRF-HR may also contribute to the
390 overestimation of fSCA over HMA in winter. Interestingly, WRF-CR simulated NSD values for
391 low fSCA case is also in better agreement with STC-MODSCAG values (Figure 3E). Winter mean
392 distribution of WRF-CR simulated fSCA over Kunlun, W.Himalaya and TP region better match
393 STC-MODSCAG values than the corresponding WRF-HR simulated fSCA values (Figure 2F). It is
394 noteworthy that these subregions (which are dominated by low fSCA grids) receive snowfall
395 from western disturbances during winter months. The cloud cover associated with the western
396 disturbances over these sub regions are extensive in winter which also introduces uncertainty

397 in MODSCAG retrievals and STC processing and contributes to the differences between WRF-HR
 398 and MODSCAG in fSCA.
 399



400

401 Figure 3: Spatial distribution of snow duration in terms of NSD from A) STC-MODSCAG
 402 retrievals. Panel B and C are similar to Panel A, but, shows number of days when fSCA is below
 403 and above 0.5 over each grid, respectively. Panels D illustrate the distribution of NSD over each
 404 sub region identified by glacier classification following Randolph Glacier Inventory. The circle
 405 and vertical legs represent mean \pm standard deviation over each region for entire year. Here,
 406 Hindu Kush, Karakoram, W.Himalayas, C.Himalayas, E.Himalayas, Tibetan Plateau, West Kunlun
 407 and East Kunlun regions are abbreviated as HK, KK, WH, CH, EH, TP, WKun and EKun,

408 respectively. Panel E and F are similar to Panel D, but, for NSD corresponding to fSCA values
409 below and above 0.5, respectively.

410

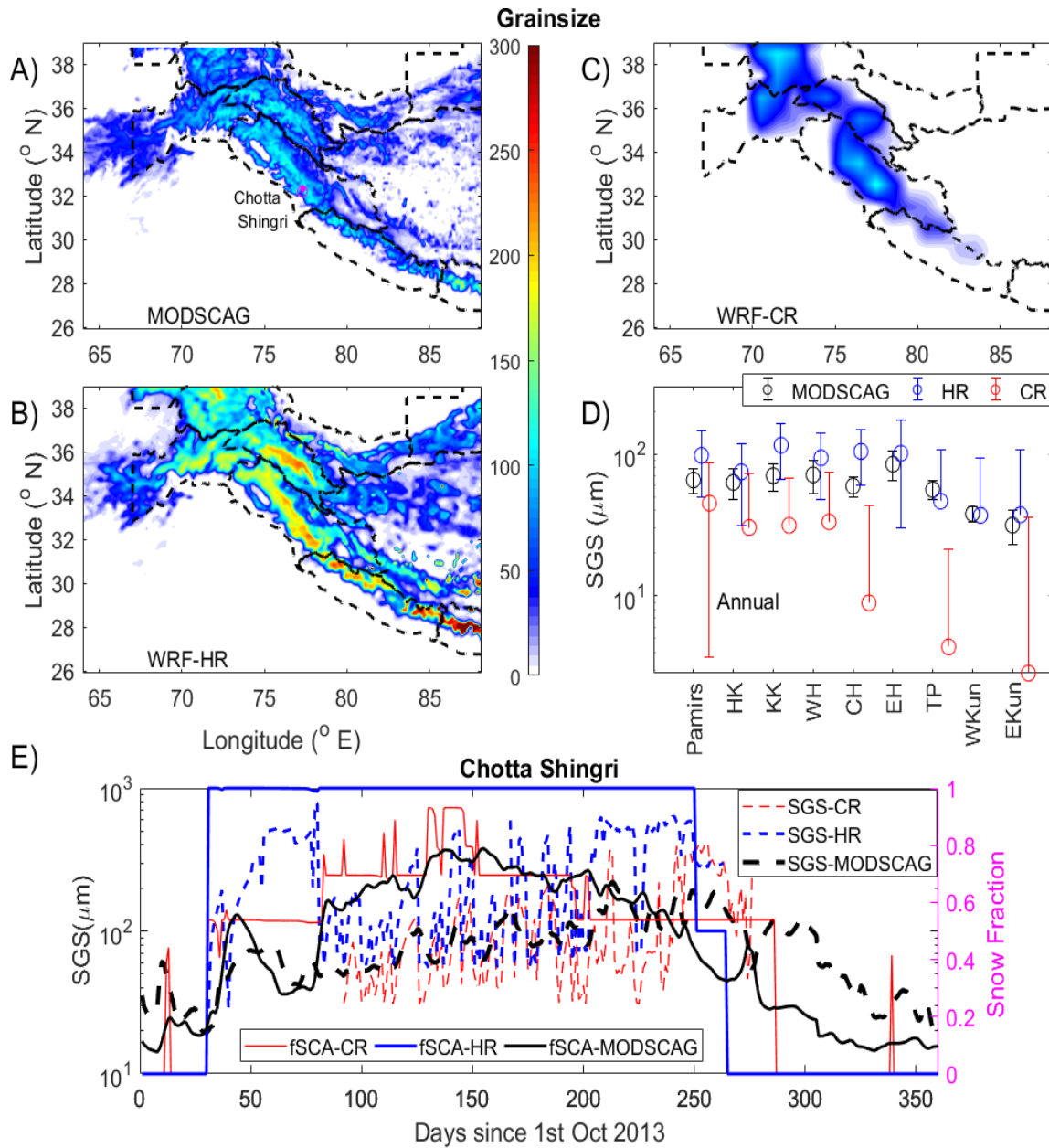
411 Comparison between performance of WRF-CR and WRF-HR for fSCA clearly show
412 significant improvements in the WRF-HR simulations over the Hindu Kush and Himalayan
413 ranges (Figure 2D). For instance, the simulated annual mean fSCA in WRF-CR around Mt.
414 Everest (shown as black circle in Figure 1) is less than 0.1 (Figure 2C). This is contrary to the high
415 fSCA values observed at Mt. Everest (0.7 in Figures 2A) and simulated by WRF-HR (0.7 in Figures
416 2B). Moreover, the improvement is present in both winter and pre-monsoon months indicating
417 it's independence from meteorological variations (Figures 2E and 2F). Analysis of NSD values
418 indicate that the snow cover duration in WRF-HR also improved significantly over these slopes
419 (Figure S4) irrespective of the season. Note that WRF-CR underestimates the snow duration
420 over Hindu Kush and Himalayas by ~2-6 months (Figure S4) and the spatial location of grids with
421 very high annual mean fSCA values (mountain ranges) improved in WRF-HR compared to the
422 STC-MODSCAG data (Figures 2A-C). The observed improvement in fSCA and NSD simulation
423 over the slopes of Himalaya and Hindu Kush can be attributed to better terrain representation
424 in WRF-HR.

425 Next, the simulated microphysical properties of the snow pack are evaluated against the
426 remote sensing retrievals. Spatial patterns in annual mean SGS from STC-MODSCAG are similar
427 to that seen in fSCA with highest values over the Karakoram and Himalayan ranges (Figures 4A)
428 corresponding to the highest elevations and likely the coldest temperatures hindering snow
429 grain growth. This spatial distribution of annual mean SGS values is well simulated in WRF-HR

430 runs (Figure 4B). But, the annual mean values over each subregion are largely overestimated by
431 30-50 micron (Figure 4D) relative to STC-MODSCAG. The seasonal distribution of region-
432 segregated SGS values from WRF-HR also compares well with that from STC-MODSCAG
433 retrievals (Figure 4E). Simulated annual mean SGS from WRF-CR (Figure 4C) lack the fine spatial
434 variability seen in STC-MODSCAG and WRF-HR. Moreover, the SGS estimates are largely
435 underestimated (by up to 100 microns) by WRF-CR specifically over grids in central and eastern
436 Himalayas, TP and Kunlun ranges (Figure 4D). The large underestimation of SGS from WRF-CR
437 and overestimation of SGS from WRF-HR is present for both pre-monsoon and winter months
438 (not shown). The overestimation of SGS from WRF-HR values corroborate well with the finding
439 that the simulated fSCA distribution from WRF-HR is largely skewed towards higher values
440 (Figure 3). Similarly, the unrealistically low mean values of SGS from WRF-CR over Himalayas, TP
441 and Kunlun ranges are consistent with the underestimation of fSCA and NSD values over these
442 regions (Figure 2 and 3). While, SGS retrievals from STC-MODSCAG are based on observed
443 surface reflectance, the modeled SGS is calculated from simulated snow mass in top model
444 layer in the grid. Hence, improvement in simulation of fSCA and NSD in high resolution WRF-HR
445 runs also caused the SGS values from WRF-HR to be closer to STC-MODSCAG retrievals than SGS
446 from WRF-CR runs. It is worth noting that the presence of cloud cover influences STC-
447 MODSCAG retrievals of SGS towards smaller grain sizes if clouds are misidentified as snow. This
448 systematic error could also contribute to the SGS differences between WRF-HR and STC-
449 MODSCAG estimates.

450

451



452

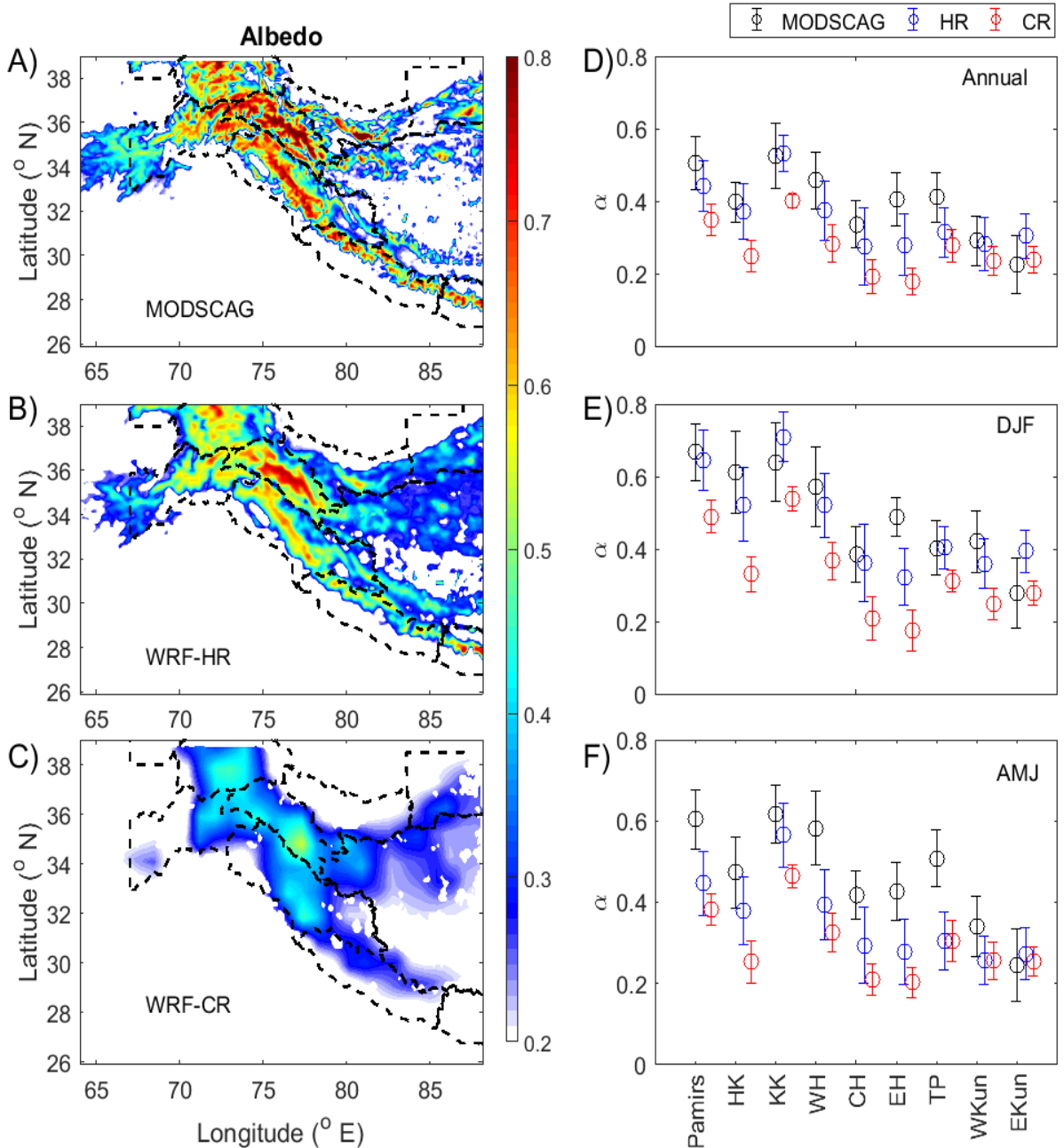
453 Figure 4: Spatial distribution of annual mean snow grain size (SGS) during midday (1000-1400
 454 LT) for water year 2013-14 from A) STC-MODSCAG retrievals and simulated values from B)
 455 WRF-HR and C) WRF-CR runs is shown. Panel D illustrates the distribution of midday mean fSCA
 456 over each subregion identified by glacier classification following Randolph Glacier Inventory.
 457 The circle and vertical legs represent mean \pm standard deviation over each region for the entire
 458 year. Here, Hindu Kush, Karakoram, W.Himalayas, C.Himalayas, E.Himalayas, Tibetan Plateau,
 459 West Kunlun and East Kunlun regions are abbreviated as HK, KK, WH, CH, EH, TP, WKun and
 460 EKun, respectively. Panel E shows time-series of daily midday SGS (hashed lines) and fSCA (solid
 461 lines) from MODSCAG (black), WRF-HR (blue) and WRF-CR (red) over a grid located near the
 462 Chotta Shingri glacier (marked by magenta diamond in Figure 3A) of western Himalaya region.

463 Quite anomalous to other grids in HMA, the WRF-CR simulated SGS values over some
464 grids near the Chotta Shingri glacier (marked by magenta circle in Figure 4A) of the western
465 Himalaya sub-region are closer to STC-MODSCAG observations than that simulated by WRF-HR
466 runs. As a sanity check, daily variation of SGS (hashed lines in Figure 4E) and fSCA (solid lines in
467 Figure 4E) from STC-MODSCAG (black), WRF-HR (blue) and WRF-CR (red) over this glacier are
468 compared. Fractional snow cover from STC-MODSCAG gradually increase from 0.2 in
469 November, 2013 to 0.8 in February, 2014 and subsequently decrease back to 0.1 by September,
470 2014 at the glacier location. Corresponding SGS values from STC-MODSCAG closely followed
471 the seasonal trend in fSCA varying around the values of 80-200 micron in winter. In comparison,
472 simulated fSCA from WRF-HR values drastically increased to 1 at the beginning of November,
473 2013 (from no snow cover before that), remained fully snow covered till mid-June, 2014 and
474 then suddenly became snow free after June. Compared to satellite estimates, fSCA from WRF-
475 HR are greater in magnitude throughout the duration of snow cover indicating more snow mass
476 simulated by WRF-HR. Associated SGS values (80-800 micron) simulated by WRF-HR are also
477 greater than STC-MODSCAG estimates throughout the snow duration over the grid. However,
478 the fSCA variation from WRF-CR over this grid is very close to the variation seen by STC-
479 MODSCAG, and the associated SGS values (50-400 micron) from WRF-CR are also closer to the
480 estimated STC-MODSCAG values, supporting our argument that biases in simulation of fSCA
481 also affect the simulated annual mean SGS values.

482 The annual mean snow albedo (α) values and the distribution over each sub region from
483 satellite estimates (by combing grain sizes from STC-MODSCAG and decrease in albedo from
484 STC-MODDRFS (see Bair et al, 2016)) and simulated by both models are presented in Figure 5.

485 Highest annual mean α values ($\sim 0.65-0.75$) are observed over mountain peaks in Karakoram,
486 Pamirs and W.Himalaya regions (Figure 5A). The location and magnitude of annual mean α over
487 these grids are closely reproduced in WRF-HR with an underestimation of $< 10\%$ (Figure 5B).
488 WRF-CR simulated annual mean α values over these grids have a considerably larger
489 underestimate of $\sim 50\%$ (Figure 5C). Similar statistics are prevalent over all the sub regions of
490 HMA (Figure 5D). Specifically, the distribution of α values from WRF-HR nearly matches the
491 observed distribution, but, the distribution of albedos from the coarser model, WRF-CR, are
492 generally 0.2-0.3 lower when compared to the observations. **The improvement of α estimation**
493 **in WRF-HR runs compared to WRF-CR runs can be attributed to the relatively better simulation**
494 **of fSCA (Figure 2), NSD (Figure 3) and SGS (Figure 4) in WRF-HR. Simulated annual mean α**
495 **values are primarily the composite albedo values of snow covered grids. In WRF-Chem-SNICAR**
496 **simulations, the composite albedo of a snow-covered grid box is computed as weighted**
497 **average of representative area fractions of sub-grid snow-cover and snow-free regions. Thus,**
498 **relatively lower values of simulated fSCA and NSD in WRF-CR runs compared to WRF-HR runs**
499 **can contribute substantially to the relatively lower annual and seasonal mean α values**
500 **simulated by WRF-CR.** Note, the opposite nature in biases simulated by WRF-HR runs in mean
501 albedo and SGS values. This is intuitive as smaller snow particles cover greater surface area and
502 therefore reflect more solar radiation from the surface. A similar pattern in distribution of snow
503 albedo from WRF-HR and WRF-CR are also found over the sub regions for pre-monsoon and
504 winter months, separately (Figures 5E and 5F), indicating robust improvement in WRF-HR
505 simulated albedo values throughout the year. The differences in simulated α in WRF-HR with
506 the observations increased during pre-monsoon and were lower during winter. Here, it is worth

507 mentioning that we are comparing instantaneous estimates obtained from Terra overpass
508 during 1000 LT with midday (1000-1400 LT) mean model values. The inherent diurnally in α
509 values under clear sky conditions in pre-monsoon season (Bair et al., 2017) might contribute
510 partially to the observed enhancement in differences during pre-monsoon season. At the same
511 time, the mean α values from STC-MODSCAG (representative of only snow covered regions) are
512 biases towards higher values than the corresponding simulated α values (composite albedo of
513 the pixel) predominantly over the snow grids with annual mean fSCA are much smaller than 1.



514

515 Figure 5: Spatial distribution of annual mean snow albedo (α) during midday (1000-1400 LT) for

516 water year 2013-14 from A) STC-MODSCAG retrievals and simulated values from B) WRF-HR

517 and C) WRF-CR runs is shown. Panels D-F illustrate the distribution of midday mean fSCA over

518 each subregion identified by glacier classification following Randolph Glacier Inventory. The

519 circle and vertical legs represent mean \pm standard deviation over each region for D) entire year,

520 E) winter (December - February) and F) pre-monsoon (April - June) season, separately. Here,

521 Hindu Kush, Karakoram, W.Himalayas, C.Himalayas, E.Himalayas, Tibetan Plateau, West Kunlun

522 and East Kunlun regions are abbreviated as HK, KK, WH, CH, EH, TP, WKun and EKun,

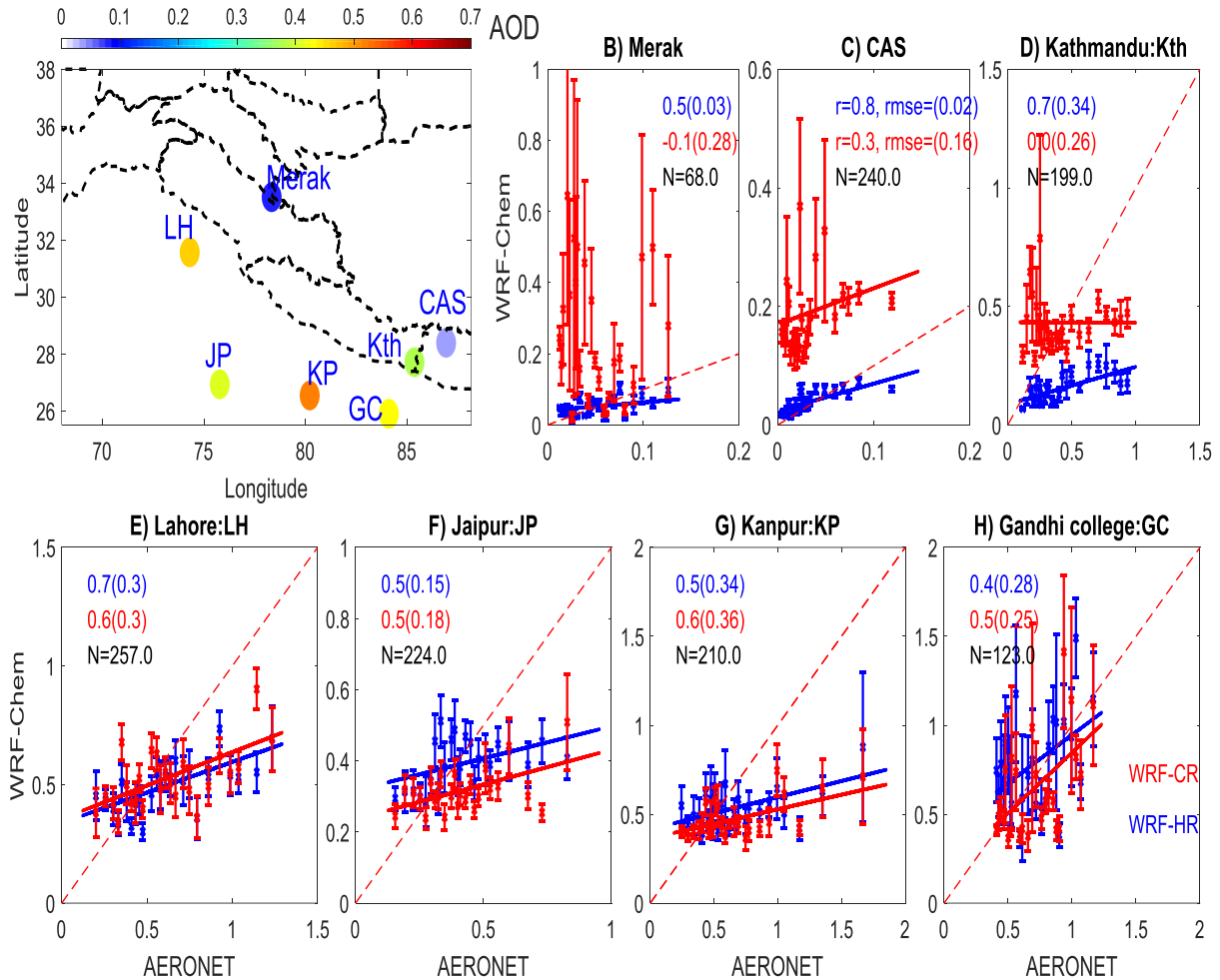
523 respectively.

524

525 **3.2: Aerosol distribution and LAP in snow**

526 We used available in-situ and ground sun photometer measurements from seven different sites
527 across our study domain (location shown in Figure 6) to evaluate the simulated aerosol optical
528 depth (AOD). The annual mean midday AOD at each site is shown in Figure 6A. Three sites (i.e.
529 Merak, CAS and Kathmandu shown in Figures 6B-D) are located on the Himalaya slopes and the
530 other four sites (Lahore, Jaipur, Kanpur and Gandhi College shown in Figures 6E-H) are located
531 in the Indo-Gangetic Plains. In-situ measurements clearly illustrate a sharp decrease (4-5 fold) in
532 mean AOD as we traverse higher up the Himalayan slope. The annual mean AOD for Lahore and
533 Kanpur sites are 0.41 and 0.52, respectively, while the AOD over high elevated sites i.e. Merak
534 and CAS sites are 0.07 and 0.05, respectively. Also, MODIS-observed AOD values prominently
535 show the reduction in annual mean AOD from the Indo-Gangetic Plains (MODIS-AOD \sim 0.4-0.7)
536 to the Tibet region (MODIS-AOD \sim 0.1-0.2) (Figure S5). Over the four sites in the Indo-Gangetic
537 Plains, AOD simulated by both WRF-HR and WRF-CR runs are well correlated with observations
538 ($r=$ 0.5-0.6, Figures 6E-6H). The biases in modelled AOD are also similar (in the range of 0.2-0.4)
539 in case of both WRF-HR and WRF-CR runs (Figures 6E-6H). Thus, no significant improvement in
540 AOD values are achieved over the plain region with fine resolution. However, distinct and large
541 improvement in simulated AOD is seen over the high elevation sites due to the increase in
542 spatial resolution. Note that AOD values from WRF-CR are not strongly correlated with
543 observations at these sites (Figures 6B-6D) and also have very high positive biases in AOD
544 values (even higher than annual mean values at Merak and CAS stations). In contrast, the
545 correlation between observations and WRF-HR is reasonably good ($r=$ 0.5-0.8 at these sites)
546 using fine spatial resolution in WRF-HR. The positive biases in AOD from WRF-HR at Merak and

547 CAS sites are lower than corresponding WRF-CR values by an order of magnitude. Presence of
548 lower biases in AOD from WRF-HR over high elevation sites indicates that the observed sharp
549 decrease in AOD values across the Himalayan slope are better captured by the higher resolution
550 WRF run (WRF-HR) than in the coarser run. Greater annual mean AOD value is simulated by
551 WRF-CR over the entire HMA region compared to WRF-HR (Figure S5) supporting an
552 overestimation of AOD from WRF-CR at higher elevation in addition to the few sites. The
553 presence of high biases (0.3-0.4) over Kathmandu valley even in WRF-HR runs indicate that
554 model resolution even finer than 12 km is likely needed to better resolve the AOD distribution
555 in complex terrain around valleys in Himalayan slope regions. **Moreover, Jayarathne et al., 2018**
556 **shows that many local emissions are not accounted in coarse emissions which causes**
557 **underestimation in simulated regional AOD values in these valleys.** Temporal variability in
558 monthly mean AOD (relatively higher AOD in pre-monsoon) is simulated reasonably well by
559 both the model versions (Figure S5).



560

561 Figure 6: Comparison of midday (averaged over 1000-1400 LT) aerosol optical depth (AOD)
 562 measured by ground based sun photometer at seven sites within the study domain with
 563 corresponding simulated AOD values from, both, WRF-HR and WRF-CR. The annual mean AOD
 564 values over each site is shown by shade in topmost left Panel. The other panels illustrates the
 565 comparison over one of each stations shown by dots in topmost left Panel. The 'N' mentioned
 566 in the legend in each panel is the total number of days when collocated data between model
 567 and measurement is available over that site. These sample points are divided into 50 equal bins
 568 of ascending AERONET-AOD values (2 percentile each) and averaged. The standard deviation in
 569 each bin is shown by the vertical bars. The correlation coefficient values (r) are also mentioned
 570 in the legend followed in brackets by the relative error values ($\sum rmse/mean\ obs$).

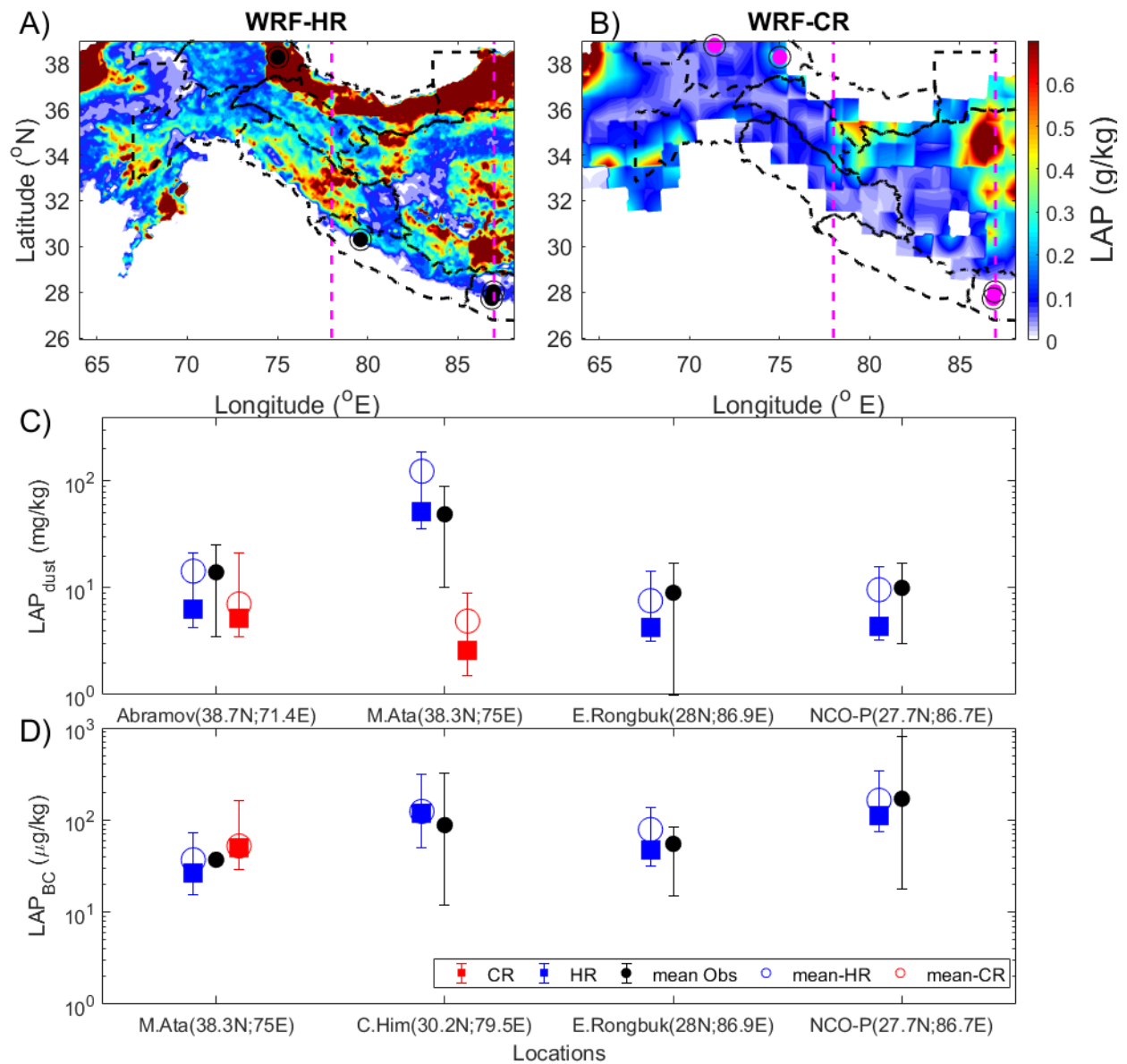
571

572

573

574

575



576

577 Figure 7: Spatial distribution of annual mean LAP concentration in snow top layer for water year
578 2013-14 simulated by A) WRF-HR and B) WRF-CR. The black dots in Panel A denote the
579 locations where observations of BC in snow is available. Similarly, the magenta dots in Panel B

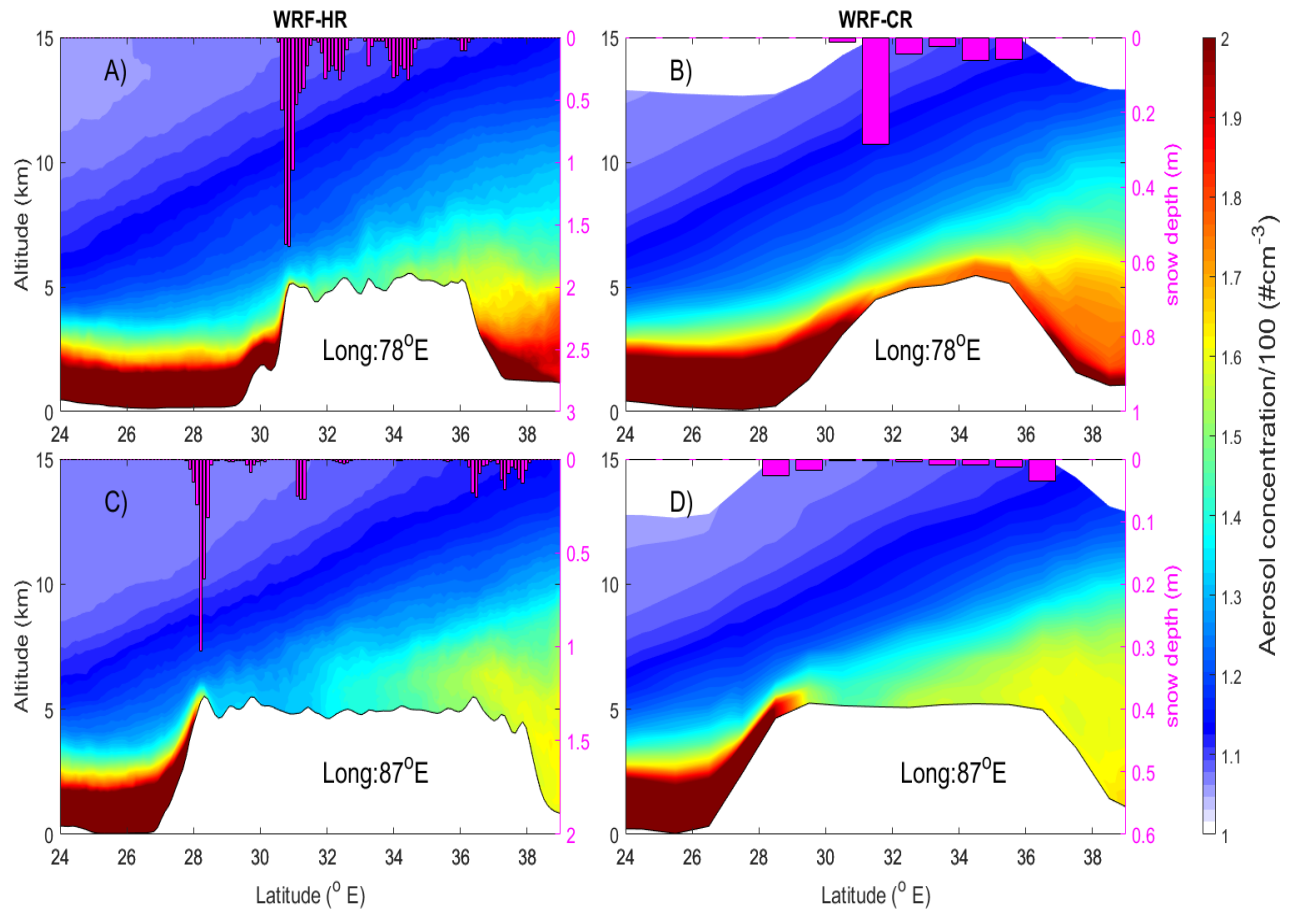
580 denote the locations from where observation of dust in snow is available. Panels C-D illustrate
581 comparison of simulated LAP_{BC} (top) and LAP_{dust} (bottom), respectively, in topmost snow layer
582 with observed values over the marked locations in the Himalayan cryosphere. **Simulated annual**
583 **mean (circle) and distribution of midday mean LAP values (box plot) is shown. The top (bottom)**
584 **edge of the box plot represent 75 (25) percentile of the distribution.** The WRF-HR and WRF-CR
585 values are represented by blue and red, respectively. The pink lines in Panel A are the cross-
586 sections shown in Figure 8.

587

588 Significant differences in simulated AOD over high elevations of Himalaya slopes and TP
589 indicate that considerable differences might also be present in LAP concentrations in snow
590 between the two WRF simulations. Annual mean LAP concentrations in top snow layer from
591 WRF-HR and WRF-CR simulations are compared in Figures 7A-7B. The comparison shows that
592 LAP concentration in WRF-HR are significantly higher than WRF-CR simulated values.
593 Quantitatively, the WRF-HR simulated annual mean LAP concentrations over the Pamir (0.5
594 g/kg), Karakoram (0.45 g/kg), Hindu Kush (0.2 g/kg), W. Himalaya (0.3 g/kg), C. Himalaya (0.2
595 g/kg) and E. Himalaya (0.08 g/kg) ranges is 3-5 times higher than the same from WRF-CR runs.
596 In contrast, WRF-HR simulated LAP over TP (0.21 g/kg) and Kunlun ranges (0.8 g/kg) is similar to
597 the mean magnitude simulated by WRF-CR runs. As a sanity check, we evaluate the simulated
598 LAP concentrations against those previously reported in the literature. Figures 7C and 7D
599 illustrate the evaluation of mean annual LAP concentration from WRF-HR and WRF-CR
600 associated with BC (LAP_{BC}) and dust (LAP_{dust}), respectively, against the reported data (shown as
601 filled black circles). The locations of reported LAP_{BC} (black filled dots) and LAP_{dust} (magenta filled
602 dots) are shown in Figure 7C and Figure 7D, respectively. First, the difference in the magnitude
603 of LAP_{dust} and LAP_{BC} over HMA is striking. The LAP_{dust} is more than 1000 times greater than
604 LAP_{BC} both in observations and the models. Secondly, LAP_{BC} and LAP_{dust} values from WRF-HR are
605 much closer to reported values compared to WRF-CR values. The differences in mean of

606 reported LAP_{BC} and LAP_{dust} distribution to that simulated by WRF-HR at various sites are in
607 range of 5-30 $\mu\text{g}/\text{kg}$ and 5-20 mg/kg , respectively. WRF-CR well simulates the concentrations of
608 LAP_{BC} and LAP_{dust} over Pamirs ($\sim 10 \text{ mg}/\text{kg}$), but significantly underestimates the LAP_{BC} and
609 LAP_{dust} (by an order of magnitude) over the Himalayan ranges. Thus, the WRF-HR better
610 simulates aerosol and LAP concentration than the WRF-CR over the HMA region.

611 It is interesting to note that finer spatial resolution resulted in lower AOD but greater
612 LAP values in snow over some places in HMA. For more insight, the vertical distribution of
613 aerosol concentration in altitude-latitude space (Figure 8) across two latitudinal cross-sections
614 (magenta colored lines in Figure 7A) is analyzed. Figure 8 illustrates the differences in simulated
615 vertical distribution of mean aerosol number concentration along 78°E (row 1) and 87°E (row 2)
616 for WRF-HR (left column) and WRF-CR (right column) runs, respectively. Corresponding terrain
617 elevation (black solid line) and snow depth (magenta bars) are also overlaid in these plots. The
618 latitude-altitude plots clearly illustrate that improved representation of the terrain in WRF-HR
619 shows the sharp change of elevation over Himalayan foothills and causes a steeper natural
620 barrier to the transport of aerosols uphill from IGP to HMA region than in the WRF-CR model.
621 Also, high spatial resolution enhances snowfall in WRF-HR over the HMA region relative to the
622 WRF-CR model. While the former change increased annual dry deposition flux, more snowfall
623 caused greater wet deposition annually in WRF-HR compared to WRF-CR (Figure S6). The
624 combination of these effects increases the deposition of aerosols and therefore LAP on the
625 southern slopes of Himalaya in the WRF-HR run. This explains the coexistence of higher LAP
626 concentration/deposition and lower AOD across HMA in WRF-HR, compared to corresponding
627 WRF-CR results.

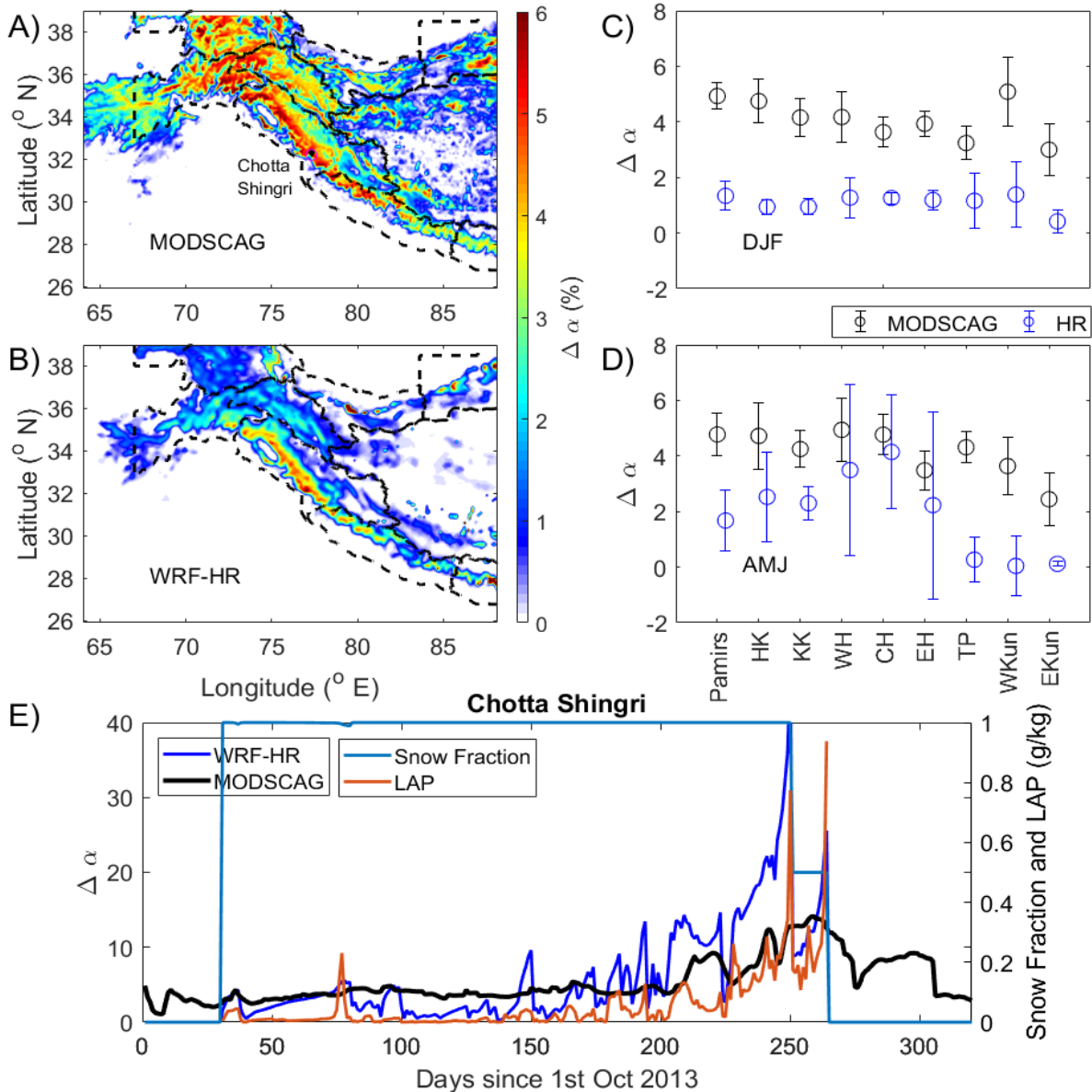


628
 629 Figure 8: Longitudinally-averaged annual mean aerosol number concentration plotted in
 630 altitude-latitude space for two longitudinal traverses across the study domain, i.e. 78°N (Panels
 631 A and B) and 87°N (Panels C and D) for both WRF-HR (left column) and WRF-CR (right column).
 632 Corresponding terrain elevation is shown in solid black line. Corresponding to each latitude, the
 633 longitudinally-averaged annual mean snow depth is also presented in magenta color bars (using
 634 y-axis on the right).

635

636

637 **3.3 LAP-induced Snow darkening and radiative forcing**



638
 639 Figure 9: Spatial distribution of annual mean LAP-induced snow albedo darkening ($\Delta\alpha$) during
 640 midday (1000-1400 LT) for water year 2013-14 from A) MODSCAG retrievals and B) simulated
 641 values from WRF-HR is shown. Panels C and D illustrate the distribution of midday mean $\Delta\alpha$
 642 over each sub region identified by glacier classification following Randolph Glacier Inventory.
 643 The circle and vertical legs represent mean \pm standard deviation over each region for entire year.
 644 Here, Hindu Kush, Karakoram, W.Himalayas, C.Himalayas, E.Himalayas, Tibetan Plateau, West
 645 Kunlun and East Kunlun regions are abbreviated as HK, KK, WH, CH, EH, TP, WKun and EKun,
 646 respectively. Panel E shows time-series of daily midday $\Delta\alpha$ from STC-MODSCAG (black) and
 647 WRF-HR (blue) over the grids located near the Chotta Shingri glacier (marked in Figure A) of
 648 western Himalaya region. Also fractional snow cover and LAP concentrations from WRF-HR over
 649 the same grids are included.

650

651 STC-MODDRFS retrievals illustrate that locations in Hindu Kush and W. Himalayas have
652 the highest annual mean LAP-induced reduction in snow albedo ($\Delta\alpha$ in %) followed by
653 Karakoram, C.Himalayas and Pamir regions (Figure 9A). WRF-HR simulated the spatial
654 variations in annual mean $\Delta\alpha$ reasonably well (Figure 9B), but, the magnitudes are
655 underestimated by ~20-40 % throughout the domain. Note that the biases in annual mean
656 values are lowest over grids in Himalayan ranges (where the underestimation is within 20%).
657 Season wise and region wise distribution plots show that the WRF-HR biases are higher in
658 winter months than the pre-monsoon months (Figures 9C and 9D). While, WRF-HR simulated
659 $\Delta\alpha$ values in the winter span between 1-3 %, the corresponding STC-MODDRFS estimates of $\Delta\alpha$
660 are larger with values ranging between 3-6% (thus no overlap with model values) over all the
661 sub regions. In pre-monsoon months, the distribution of modeled WRF-HR $\Delta\alpha$ values over
662 Karakoram and Himalayan ranges are similar in magnitude, explaining the lower biases in
663 annual mean values over Himalayas. This spatiotemporal variability in differences between STC-
664 MODDRFS retrievals and simulated $\Delta\alpha$ values is consistent with the variability in biases of
665 fractional snow cover seen in WRF-HR (Figures 2E and 2F). For a closer look, the difference in
666 daily midday mean $\Delta\alpha$ values from STC-MODDRFS (black) and WRF-HR (blue) are compared (in
667 Figure 9E) over the grids of Chotta Shingri glacier (similar as Figure 4E). Corresponding, midday
668 mean fSCA (light blue) and LAP (orange) from WRF-HR are also plotted. $\Delta\alpha$ values from STC-
669 MODDRFS are about 5% during winter months, but, increases in pre-monsoon months until
670 mid-June (peak value is 18%). Albedo reduction is closely associated with the temporal
671 progression in midday LAP concentration in snow over this region at daily scale. In agreement,
672 midday $\Delta\alpha$ values from WRF-HR are lower in winter months and higher in pre-monsoon

673 months. Except occasional peaks, with magnitudes of 3-4 %, $\Delta\alpha$ values from WRF-HR largely
674 remained below 3 % till late February. A steep increase in $\Delta\alpha$ values from WRF-HR is seen in
675 March (monthly mean \sim 4%), April (9%), May (13%) and June (18%).

676 As already discussed, the simulated fSCA values in WRF-HR are greater than observed
677 fSCA from STC-MODSCAG for most of the winter season (Figure 4E). Specifically, the
678 underestimation in WRF-HR simulated $\Delta\alpha$ values (Figures 9C and 9D) in winter over Karakoram,
679 Hindu Kush and Himalayas is in agreement with corresponding overestimation of WRF-HR
680 simulated fSCA values over these regions (Figure 2). STC-MODDRFS estimated $\Delta\alpha$ is based on
681 surface reflectance, while $\Delta\alpha$ calculated by model involves the surface layer depth. The surface
682 snow layer in SNICAR/CLM continuously evolves as fresh snowfall is added or with snow
683 melting, so the LAP concentrations in the surface layer depend on new snowfall, meltwater
684 flushing, and layer combination/division (Flanner et al., 2007; Flanner et al., 2012; Oleson et al.,
685 2010). Therefore, more precipitation and more snow coverage in winter can be a primary factor
686 causing the underestimation of annual mean LAP concentration and LAP-induced snow
687 darkening. Secondly, the associated overestimation in simulated SGS during winter (Figure 4)
688 can also contribute to the lower $\Delta\alpha$ values simulated in WRF-HR because bigger snow grains in
689 WRF-HR lead to lower clean albedo and thus smaller percentage reduction in albedo compared
690 to STC-MODDRFS. Moreover, we have assumed spherical shaped snow grains in our
691 simulations. Recently, microscopic level studies show that uncertainties associated with
692 simplified snow grain shape treatment in model parameterization can solely contribute to large
693 biases in SNICAR- $\Delta\alpha$ estimates and thus the LAP-snow albedo radiative and snow melt feedback
694 processes (Liou et al., 2014; Dang et al., 2016; He et al., 2017). Thirdly, the fact that the

695 persistent cloud cover over HMA during winter season can induces a lot of uncertainty in the
696 STC-MODSCAG and STC-MODDRFS estimates, is also equally important.

697 At the same time, uncertainties regarding aerosol emission, transport and deposition to
698 the snow layers are also significant. It is well known that the transport and deposition of black
699 carbon from Indian landmass to Himalayas increases in the afternoon with the evolution of
700 boundary layer over the IGP region (Dumka et al., 2015; Raatikainen et al., 2014). This feature is
701 well simulated by the model (not shown). As STC-MODDRFS estimates are representative of
702 1000 LT, but simulated values are sampled in the midday (1000-1400 LT), positive biases in
703 aerosol transport and deposition in snow packs (i.e. higher $\Delta\alpha$ values) might be simulated in
704 WRF-HR runs, especially during pre-monsoon months. At the same time, GOCART dust emission
705 parameterization (used here) is dependent on near surface wind speed. Previous studies have
706 evaluated and illustrated inherent uncertainties in dust emission by this parameterization,
707 mostly underestimation over Indian region (Dipu et al., 2013; Kumar et al., 2014). Thus, the
708 uncertainty in local dust emission fluxes over HMA can also contribute to the biases in
709 simulated $\Delta\alpha$ values. Also, large biases in LAP values may be simulated due to model
710 uncertainties in enhanced wet scavenging fluxes in winter. An overestimation in LAP
711 concentration can lead to an overestimation of snow darkening and melting, resulting in an
712 underestimation of NSD (Figure S4). The large biases in $\Delta\alpha$ values (> 20 %) simulated by WRF-HR
713 towards late spring could be attributed to both, underestimation in fSCA and overestimation of
714 LAP concentration in the model.

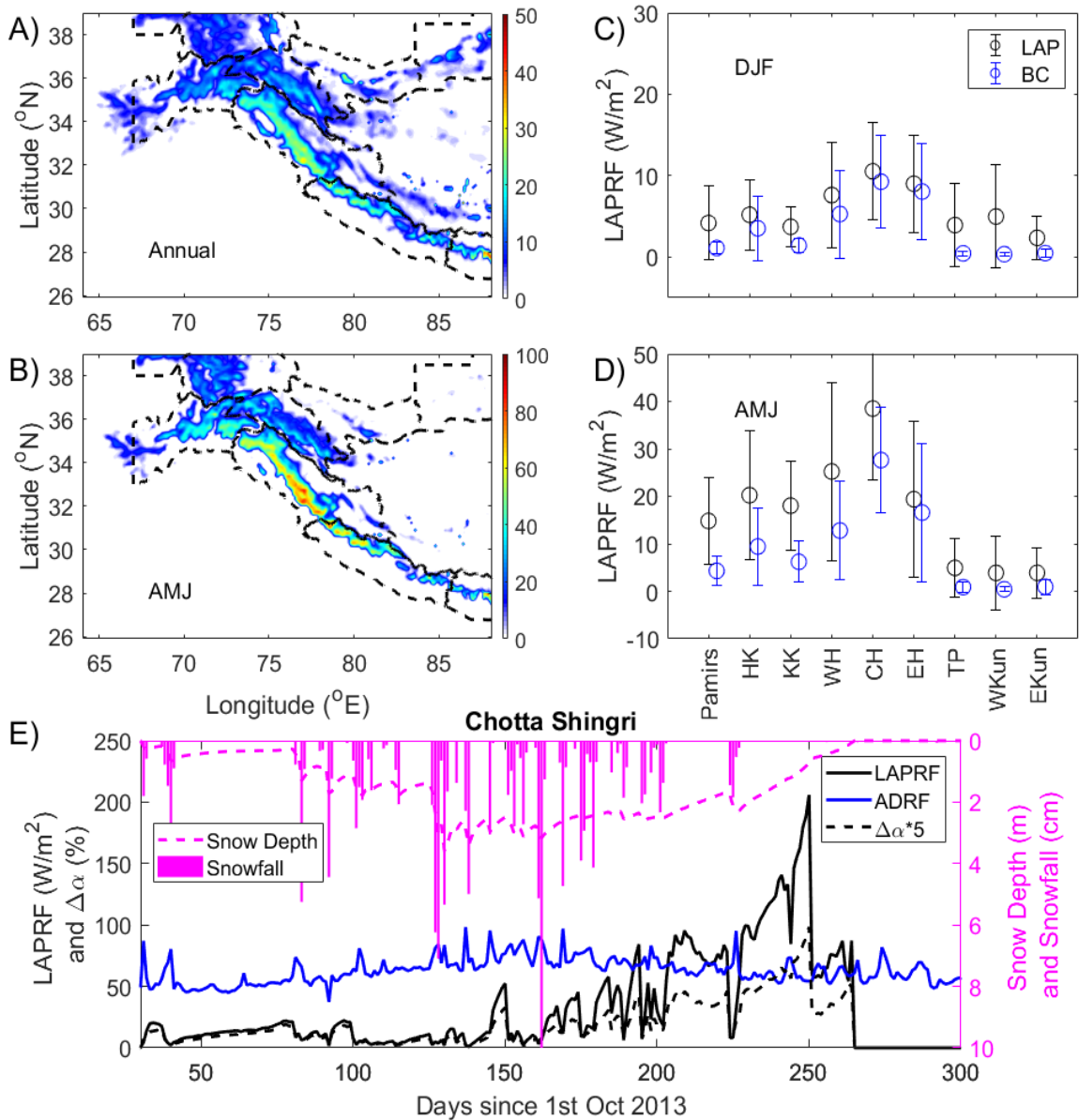
715 Although a better quantification of these model biases requires evaluation against in-
716 situ measurements, it is worth mentioning here that no in-situ measurements are available for

717 a direct comparison of these high $\Delta\alpha$ values WRF-HR over W. Himalayas (Gertler et al., 2016).
718 Nonetheless, the high values simulated during pre-monsoon are close to previously reported
719 values over other HMA regions. Kaspari et al., (2014) used the offline SNICAR model to report
720 that BC concentrations in pre-monsoon snow/ice samples at Mera Glacier were large enough to
721 reduce albedo by 6-10% and the reduction in albedo was 40-42% relative to clean snow when
722 dust is included in the calculation. Recently, Zhang et al. (2018) has combined a large dataset of
723 LAP measurements in surface snow with the offline SNICAR model to illustrate that $\Delta\alpha$ can be
724 >35% over Tibetan Plateau. Moreover, the composite effect of this discrepancy on
725 seasonal/annual mean values is minimal as the snowpack is at its minimum near the end of pre-
726 monsoon season. Similar high daily variability, huge radiative forcing values (LAPRF ~200
727 W/m²) and sudden decline in snow depth in late pre-monsoon is also reported over upper
728 Colorado river basin (Skiles et al., 2015; Skiles and Painter, 2017)

729

730

731



732
 733 Figure 10: A) Spatial distribution of annual mean snow mediated LAP-induced radiative forcing
 734 (LAPRF) from WRF-HR and B) Spatial distribution of seasonal mean LAPRF over snow covered
 735 for pre-monsoon season (AMJ) of water year 2013-14. Panels C and D illustrate the distribution
 736 of LAPRF (blue) and BC-only-LAPRF (black) over each sub region identified by glacier
 737 classification following Randolph Glacier Inventory for winter and pre-monsoon, respectively.
 738 The circle and vertical legs represent mean \pm standard deviation over each region for entire year.
 739 Here, Hindu Kush, Karakoram, W.Himalayas, C.Himalayas, E.Himalayas, Tibetan Plateau, West
 740 Kunlun and East Kunlun regions are abbreviated as HK, KK, WH, CH, EH, TP, W.Kun and E.Kun,
 741 respectively. Panel E shows time-series of daily midday LAPRF (blue) and aerosol direct
 742 radiative forcing at surface (ADRF, blue) over the Chotta Shingri region (marked in Figure 9A) of
 743 western Himalaya region. The simulated LAP-induced change in snow albedo is also shown in
 744 hashed black line. Also snow depth and snowfall from WRF-HR over the same grid is included.

745 In agreement with the spatial variation in $\Delta\alpha$ values, the annual mean snow-mediated
746 LAP-induced radiative forcing (LAPRF) from WRF-HR over grids in W.Himalayas and C. Himalayas
747 are highest followed by Karakoram, Hindu Kush, E.Himalayas and Pamir regions (Figure 10A).
748 The spatial distribution of pre-monsoon mean LAPRF values from WRF-HR (Figure 10B) is similar
749 to that of the annual mean LAPRF values, but, the pre-monsoon magnitudes are higher by an
750 order of magnitude throughout most of the domain. This is mainly due to the large increase in
751 $\Delta\alpha$ values in pre-monsoon when LAPs aggregate on the surface compared with winter months
752 when LAPs are continuously covered by new snow (Figure 9). Spatio-temporal variability in
753 LAPRF is evident in the seasonal and regional distribution plots (Figure 10C and 10D). LAPRF
754 values over the edges of HMA are greater than the highland TP region in both winter and pre-
755 monsoon months probably due to greater LAP deposition simulated over Hindu Kush,
756 Karakoram and Himalayas regions (Figure S7) from the close proximity of dust sources. Also, it
757 is clearly visible that the maximum LAPRF values within HMA region are present over grids in
758 Himalayan ranges (during both winter and pre-monsoon) with annual mean values $> 50 \text{ W/m}^2$
759 (seen in Figures 10B and 10D) and maximum instantaneous values higher than 150 W/m^2 (not
760 shown). The time series of midday mean LAPRF values (Figure 10E) over the same grids in the
761 Chotta Shingri Glacier region in western Himalaya is plotted to ascertain possible daily
762 variability in LAPRF for midday over the region. Corresponding LAP-induced albedo reduction,
763 snow depth and snowfall values are also plotted to show how LAPRF can affect local snow
764 melting. The daily snow depth increases to 3.6 m in winter (30-150 days) followed by gradual
765 reduction and snow cover melting in pre-monsoon (150-270 days). The mean midday LAPRF
766 value is $\sim 10 \text{ W/m}^2$ in winter season, but, the magnitude increased gradually during March (18

767 W/m^2), April ($44 W/m^2$), May ($86 W/m^2$) and June ($123.5 W/m^2$), eventually terminating with a
768 peak value of $202 W/m^2$ in mid-June. The temporal evolution in $\Delta\alpha$ values closely followed the
769 LAPRF values with a variation in range of 1-20%. The shortwave aerosol direct radiative forcing
770 (ADRF) during midday at the surface over the same grid is also shown (as blue curve) in
771 Figure10E. The momentarily high values of ADRF during the period indicate dust storms or
772 sudden increase in aerosol loading over the grid. A closer look illustrate that the large daily
773 variations in LAPRF and $\Delta\alpha$ are associated with the variability in ADRF and daily snowfall
774 occurrence over the grid. Fresh snowfall feedbacks result in subsequent reduction in LAPRF and
775 enhancement in snow depth (Figure10E), while, higher aerosol loading over aged snow is
776 followed by a clear increase in LAPRF. During melting, our model considers that only a fraction
777 of LAP is washed away with meltwater, which, results in enhanced concentration of LAP during
778 the end stages of the snowpack. This snow albedo feedback along with the momentary high
779 aerosol loading (on 250th day) can explain the very high values of albedo reduction and LAPRF
780 that were simulated during the last days of the snow cover over this grid. Higher LAPRF values
781 indicate more energy being absorbed by the snow pack and thus more snow melting.
782 Therefore, LAP-induced snow melting effect over Himalaya is very significant and is the largest
783 relative to other areas within HMA.

784 Snow-mediated radiative forcing only due to BC- deposition is shown in Figures10C and
785 10D. Although, similar spatiotemporal pattern in LAPRF and BC-only-LAPRF is simulated,
786 contrasting features in context to BC contribution to LAPRF are present in between the western
787 part and eastern parts of HMA. During winter, the magnitude of BC-only LAPRF values is similar
788 to that of total LAPRF over the western part of HMA region (i.e. Pamirs, Karakoram, Hindu Kush

789 and W.Himalayas) suggesting that BC is a dominant contributor to net LAPRF (Figures10C). But,
790 large differences between LAPRF and BC-only LAPRF is present during pre-monsoon season
791 over the western regions indicating that dust contribution is more or less equal to that of BC
792 contribution over these regions (Figure10D). In contrast, the dust contribution to LAPRF values
793 over the eastern domain (TP and Kunlun regions) is significant during winter season (Figures10C
794 and 10D). The spatiotemporal variability in dust and BC contribution is reported previously and
795 is mainly linked with the seasonal variability in meteorology and associated advection of South
796 Asian emissions (Zhang et al., 2015; Wang et al., 2015a ; Niu et al., 2018). The ADRF-induced
797 surface cooling effect may nullify the effects of LAPRF-induced warming effect on snowpack
798 melting. But, the drastic increase in LAPRF values in April through June causes the magnitude of
799 LAPRF to be twice that of ADRF over W. Himalayas during snow melting period, highlighting
800 dominance of LAPRF (as also seen in Figure10E).

801 The simulated annual mean, pre-monsoon mean and BC-only-LAPRF values from WRF-
802 HR are in general, higher compared to previously reported estimates of LAPRF from model
803 studies at coarser resolution. For example, Ménégos et al., (2014) have reported annual mean
804 LAPRF of $\sim 1-3 \text{ W/m}^2$ over Himalaya using an online simulation at 50 km resolution grid.
805 Similarly, Qian et al., (2011) used the Community Atmosphere Model version 3.1 at coarser
806 spatial resolution to show that simulated aerosol-induced snow albedo perturbations can
807 generate LAPRF values of $5-25 \text{ W/m}^2$ during pre-monsoon over HMA. Also, coarsely resolved
808 GEOS-Chem runs simulated BC-only-LAPRF can vary from 5 to 15 W/m^2 in the snow-covered
809 regions over the TP (Kopacz et al., 2011). Recently, a decade long simulation using the RegCM
810 model at 50 km spatial resolution also estimated maximum BC-only-LAPRF values of $5-6 \text{ W/m}^2$

811 over the Himalaya and southeastern TP averaged over non-monsoon season (Ji, 2016).
812 However, the comparison of WRF-HR and WRF-CR simulations provided in this study clearly
813 show that the magnitudes of snow macro- and micro-properties, aerosol loading and LAP-
814 induced albedo darkening over Himalayas improved significantly with finer spatial resolution.
815 Thus, the global model simulated LAPRF values are likely underestimated. In agreement,
816 recently, Zhang et al., (2018) has estimated BC-only-LAPRF of 20-35 W/m² using offline SNICAR
817 calculation forced with a greater coverage of measurements of surface snow content. He et al.,
818 (2018) have also reported similar high BC-only-LAPRF values after implementing a realistic snow
819 grainsize parameterizations in offline SNICAR calculations over HMA.

820

821

822 **4. Summary and Implications**

823 In this study, we use the SNICAR model coupled with WRF-Chem regional model at high spatial
824 resolution (WRF-HR; 12 km) to simulate the transport, deposition, and radiative forcing of light
825 absorbing particles (LAPs; mainly Black Carbon and dust) over the high mountains of Asia (HMA)
826 during water year 2013-14. The snow grain sizes and LAP-induced snow darkening was
827 evaluated, for the first time, against comprehensive satellite retrievals (the MODSCAG and
828 MODDRFS spatial and temporally complete retrieved satellite observations) over HMA. The
829 atmospheric aerosol loading is evaluated against satellite and ground-based AOD
830 measurements over HMA region. Results from another simulation which employ the same
831 model configuration but a coarser spatial resolution (WRF-CR; 1 degree) are also compared

832 with WRF-HR to illustrate the significance of a better representation of terrain on snow-pack
833 and aerosol simulation over HMA. The main conclusions from our study are:

834a) The simulated macro- and micro-physical properties and the duration of snow packs over HMA
835 improve significantly due to the use of fine spatial resolution, especially over the southern
836 slopes of Hindu Kush and Himalayan ranges.

837b) Simulated aerosol loading over HMA is also more realistic in WRF-HR than in WRF-CR, which
838 leads to a reduction in biases of annual mean LAP concentration in snow. This improvement is
839 attributed to a more realistic simulation of wet deposition (due to a better simulation of snow
840 pack) and dry deposition of LAPs (associated with a better representation of terrain) in WRF-HR.

841c) WRF-HR captures the magnitude of LAP-induced snow albedo reduction ($\Delta\alpha$) over Himalayas
842 and Hindu Kush region relatively well compared to the STC-MODDRFS retrievals during pre-
843 monsoon. However, during winter, large biases in modelled $\Delta\alpha$ values are present. This is
844 probably due to inherent uncertainties in model parameterizations and satellite retrievals
845 associated with the cloud cover over HMA in winter period.

846d) The glaciers and snow cover regions located in the Himalaya have the highest LAPRF within
847 HMA i.e. annual mean LAPRF $\sim 20 \text{ W/m}^2$ and pre-monsoon mean LAPRF $\sim 40 \text{ W/m}^2$. This is
848 consistent with similar high values of $\Delta\alpha$ over Himalayan ranges i.e. annual mean $\Delta\alpha$ values ~ 2 -
849 4 % and pre-monsoon mean $\Delta\alpha$ values ~ 4 -8 %. The annual mean LAP concentration in snow
850 values (200-300 mg/kg) are also high. Thus, the Himalaya (more specifically, western Himalayas)
851 is most vulnerable to LAP-induced snow melting within HMA.

852

853 Ramanathan and G. Carmichael, (2008) suggest that atmospheric warming from LAPs
854 ($\sim 20 \text{ W/m}^2$) may be just as important as greenhouse gases in the melting of snowpack and
855 glaciers over Asia. In this context, the high magnitudes of LAPRF values in pre-monsoon over
856 HMA ($\sim 40 \text{ W/m}^2$) clearly shows that snow-mediated aerosol forcing on snow melting over HMA
857 can be twofold the significance of the atmospheric forcing. Nonetheless, the differences in
858 snow surface properties between WRF-HR and satellite observations indicate probable
859 uncertainties in model parameterizations. At the same time, the STC-MODDRFS retrievals
860 themselves may have an uncertainty of $\sim 5\%$ in instantaneous $\Delta\alpha$ measurements. Thus, efforts
861 to further reducing the LAPRF uncertainties in the model are warranted in the future by using
862 in-situ observations (i.e. field campaigns), specifically over the most affected western
863 Himalayas, where relevant measurements are largely absent (Gertler et al., 2016). Moreover,
864 satellite retrievals will be markedly improved in the coming decade with the NASA Decadal
865 Survey Surface Biology and Geology imaging spectrometer mission, which includes as a core
866 measurement snow albedo and its controls (National Academies of Science, 2018). These
867 visible through shortwave infrared imaging spectrometer retrievals have uncertainties an order
868 of magnitude smaller (Painter et al., 2013) than those from multispectral sensors such as
869 MODIS and will provide a more accurate constraint on the physically-based modeling pursued
870 here.

Author contribution:

CS and YQ conceptualized the study. CS did the modeling, analysis and wrote the paper under the supervision of YQ. KR, KB and TP created the STC-MODSCAG and STC-MODDRFS datasets. All authors provided advice and feedback throughout the analysis, drafting and submission process.

Acknowledgment

This research was supported by the NASA High Mountain Asia Project. The Pacific Northwest National Laboratory (PNNL) is operated for DOE by Battelle Memorial Institute under contract DE-AC06-76RLO 1830. Part of this work was performed at the Jet Propulsion Laboratory, California Institute of Technology under contract with NASA. H. Wang acknowledges support from the U.S. Department of Energy (DOE), Office of Science, Biological and Environmental Research as part of the Earth System Modeling program. We thank the PIs of the selected AERONET and SKYNET stations, for providing the data used in this study. The AERONET data are obtained from the AERONET website, <http://aeronet.gsfc.nasa.gov/>. We also thank the PI of the selected SkyNet station, for providing the data used in this study. The SkyNet data is obtained from the website <http://atmos3.cr.chiba-u.jp/skynet/merak/merak.html/>.

References

- Amante, C. and Eakins, B. W.: ETOPO1 1 Arc-Minute Global Relief Model: Procedures, Data Sources and Analysis., 2009.
- Azam, M. F., Ramanathan, A., Wagnon, P., Vincent, C., Linda, A., Berthier, E., Sharma, P., Mandal, A., Angchuk, T., Singh, V. B. and Pottakkal, J. G.: Meteorological conditions, seasonal and annual mass balances of Chhota Shigri Glacier, western Himalaya, India, *Ann. Glaciol.*, 57(71), 328–338, doi:10.3189/2016AoG71A570, 2016.
- Bair, E. H., Rittger, K., Davis, R. E., Painter, T. H. and Dozier, J.: Validating reconstruction of snow water equivalent in California's Sierra Nevada using measurements from the NASA Airborne Snow Observatory, *Water Resour. Res.*, 52(11), 8437–8460, doi:10.1002/2016WR018704, 2016.
- Barnard, J. C., Fast, J. D., Paredes-Miranda, G., Arnott, W. P. and Laskin, A.: Technical note: Evaluation of the WRF-Chem "Aerosol chemical to aerosol optical properties" module using data from the MILAGRO campaign, *Atmos. Chem. Phys.*, 10(15), 7325–7340, doi:10.5194/acp-10-7325-2010, 2010.
- Barnett, T. P., Adam, J. C. and Lettenmaier, D. P.: Potential impacts of a warming climate on water availability in snow-dominated regions, *Nature*, 438(7066), 303–309,

doi:10.1038/nature04141, 2005.

Binkowski, F. S. and Shankar, U.: The Regional Particulate Matter Model. 1. Model description and preliminary results, *J. Geophys. Res.*, 100(D12), 26191–26209, doi:10.1029/95JD02093, 1995.

Bolch, T., Kulkarni, A., Käab, A., Huggel, C., Paul, F., Cogley, J. G., Frey, H., Kargel, J. S., Fujita, K., Scheel, M., Bajracharya, S. and Stoffel, M.: The state and fate of himalayan glaciers, *Science* (80- .), 336(6079), 310–314, doi:10.1126/science.1215828, 2012.

Bollasina, M. A., Ming, Y. and Ramaswamy, V.: Anthropogenic Aerosols and the Weakening of the South Asian Summer Monsoon, *Science* (80- .), 334(6055), 502–505, doi:10.1126/science.1204994, 2011.

Bonasoni, P., Laj, P., Marinoni, A., Sprenger, M., Angelini, F., Arduini, J., Bonafè, U., Calzolari, F., Colombo, T., Decesari, S., Di Biagio, C., Di Sarra, A. G., Evangelisti, F., Duchi, R., Facchini, M. C., Fuzzi, S., Gobbi, G. P., Maione, M., Panday, A., Roccatò, F., Sellegri, K., Venzac, H., Verza, G. P., Villani, P., Vuillermoz, E. and Cristofanelli, P.: Atmospheric Brown Clouds in the Himalayas: First two years of continuous observations at the Nepal Climate Observatory-Pyramid (5079 m), *Atmos. Chem. Phys.*, 10(15), 7515–7531, doi:10.5194/acp-10-7515-2010, 2010.

Bond, T. C., Doherty, S. J., Fahey, D. W., Forster, P. M., Berntsen, T., Deangelo, B. J., Flanner, M. G., Ghan, S., Kärcher, B., Koch, D., Kinne, S., Kondo, Y., Quinn, P. K., Sarofim, M. C., Schultz, M. G., Schulz, M., Venkataraman, C., Zhang, H., Zhang, S., Bellouin, N., Guttikunda, S. K., Hopke, P. K., Jacobson, M. Z., Kaiser, J. W., Klimont, Z., Lohmann, U., Schwarz, J. P., Shindell, D., Storelvmo, T., Warren, S. G. and Zender, C. S.: Bounding the role of black carbon in the climate system: A scientific assessment, *J. Geophys. Res. Atmos.*, 118(11), 5380–5552, doi:10.1002/jgrd.50171, 2013.

Brandt, R. E., Warren, S. G. and Clarke, A. D.: A controlled snowmaking experiment testing the relation between black carbon content and reduction of snow albedo, *J. Geophys. Res. Atmos.*, 116(8), doi:10.1029/2010JD015330, 2011.

Brown, R. D. and Robinson, D. A.: Northern Hemisphere spring snow cover variability and change over 1922–2010 including an assessment of uncertainty, *Cryosphere*, 5(1), 219–229, doi:10.5194/tc-5-219-2011, 2011.

Campanelli, M., Estellés, V., Tomasi, C., Nakajima, T., Malvestuto, V. and Martínez-Lozano, J. A.: Application of the SKYRAD Improved Langley plot method for the in situ calibration of CIMEL Sun-sky photometers., *Appl. Opt.*, 46(14), 2688–702, doi:10.1364/AO.46.002688, 2007.

Chapman, E. G., Gustafson, W. I., Easter, R. C., Barnard, J. C., Ghan, S. J., Pekour, M. S. and Fast, J. D.: Coupling aerosol-cloud-radiative processes in the WRF-Chem model: Investigating the radiative impact of elevated point sources, *Atmos. Chem. Phys.*, 9(3), 945–964, doi:10.5194/acp-9-945-2009, 2009.

Conway, H., Gades, A. and Raymond, C. F.: Albedo of dirty snow during conditions of melt, *Water Resour. Res.*, 32(6), 1713–1718, doi:10.1029/96WR00712, 1996.

- Dang, C., Warren, S. G., Fu, Q., Doherty, S. J., Sturm, M. and Su, J.: Measurements of light-absorbing particles in snow across the Arctic, North America, and China: Effects on surface albedo, *J. Geophys. Res. Atmos.*, 122(19), 10149–10168, doi:10.1002/2017JD027070, 2017.
- Dentener, F., Kinne, S., Bond, T., Boucher, O., Cofala, J., Generoso, S., Ginoux, P., Gong, S., Hoelzemann, J. J., Ito, A., Marelli, L., Penner, J. E., Putaud, J. P., Textor, C., Schulz, M., Van Der Werf, G. R. and Wilson, J.: Emissions of primary aerosol and precursor gases in the years 2000 and 1750 prescribed data-sets for AeroCom, *Atmos. Chem. Phys.*, 6(12), 4321–4344, doi:10.5194/acp-6-4321-2006, 2006.
- Doherty, S. J., Warren, S. G., Grenfell, T. C., Clarke, A. D. and Brandt, R. E.: Light-absorbing impurities in Arctic snow, *Atmos. Chem. Phys.*, 10(23), 11647–11680, doi:10.5194/acp-10-11647-2010, 2010.
- Doherty, S. J., Grenfell, T. C., Forsström, S., Hegg, D. L., Brandt, R. E. and Warren, S. G.: Observed vertical redistribution of black carbon and other insoluble light-absorbing particles in melting snow, *J. Geophys. Res. Atmos.*, 118(11), 5553–5569, doi:10.1002/jgrd.50235, 2013.
- Dozier, J., Painter, T. H., Rittger, K. and Frew, J. E.: Time-space continuity of daily maps of fractional snow cover and albedo from MODIS, *Adv. Water Resour.*, 31(11), 1515–1526, doi:10.1016/j.advwatres.2008.08.011, 2008.
- Dubovik, O., Smirnov, A., Holben, B. N., King, M. D., Kaufman, Y. J., Eck, T. F. and Slutsker, I.: Accuracy assessments of aerosol optical properties retrieved from Aerosol Robotic Network (AERONET) Sun and sky radiance measurements, *J. Geophys. Res. Atmos.*, 105(D8), 9791–9806, doi:10.1029/2000JD900040, 2000.
- Dyurgerov, M. B.: Mountain glaciers at the end of the twentieth century: Global analysis in relation to climate and water cycle, *Polar Geogr.*, 25(4), 241–336, doi:10.1080/10889370109377717, 2001.
- Easter, R. C., Ghan, S. J., Zhang, Y., Saylor, R. D., Chapman, E. G., Laulainen, N. S., Abdul-Razzak, H., Leung, L. R., Bian, X. and Zaveri, R. A.: MIRAGE: Model description and evaluation of aerosols and trace gases, *J. Geophys. Res. D Atmos.*, 109(20), doi:10.1029/2004JD004571, 2004.
- Fan, J., Wang, Y., Rosenfeld, D. and Liu, X.: Review of Aerosol–Cloud Interactions: Mechanisms, Significance, and Challenges, *J. Atmos. Sci.*, 73(11), 4221–4252, doi:10.1175/JAS-D-16-0037.1, 2016.
- Fast, J. D., Gustafson, W. I., Easter, R. C., Zaveri, R. A., Barnard, J. C., Chapman, E. G., Grell, G. A. and Peckham, S. E.: Evolution of ozone, particulates, and aerosol direct radiative forcing in the vicinity of Houston using a fully coupled meteorology-chemistry-aerosol model, *J. Geophys. Res. Atmos.*, 111(21), doi:10.1029/2005JD006721, 2006.
- Flanner, M. G. and Zender, C. S.: Snowpack radiative heating: Influence on Tibetan Plateau climate, *Geophys. Res. Lett.*, 32(6), 1–5, doi:10.1029/2004GL022076, 2005.
- Flanner, M. G., Zender, C. S., Randerson, J. T. and Rasch, P. J.: Present-day climate forcing and response from black carbon in snow, *J. Geophys. Res. Atmos.*, 112(11),

doi:10.1029/2006JD008003, 2007.

Flanner, M. G., Zender, C. S., Hess, P. G., Mahowald, N. M., Painter, T. H., Ramanathan, V. and Rasch, P. J.: Springtime warming and reduced snow cover from carbonaceous particles, *Atmos. Chem. Phys.*, 9(7), 2481–2497, doi:10.5194/acp-9-2481-2009, 2009.

Flanner, M. G., Liu, X., Zhou, C., Penner, J. E. and Jiao, C.: Enhanced solar energy absorption by internally-mixed black carbon in snow grains, *Atmos. Chem. Phys.*, 12(10), 4699–4721, doi:10.5194/acp-12-4699-2012, 2012.

Gautam, R., Hsu, N. C., Lau, W. K. M. and Yasunari, T. J.: Satellite observations of desert dust-induced Himalayan snow darkening, *Geophys. Res. Lett.*, 40(5), 988–993, doi:10.1002/grl.50226, 2013.

Gertler, C. G., Puppala, S. P., Panday, A., Stumm, D. and Shea, J.: Black carbon and the Himalayan cryosphere: A review, *Atmos. Environ.*, 125, 404–417, doi:10.1016/j.atmosenv.2015.08.078, 2016.

Ghatak, D., Sinsky, E. and Miller, J.: Role of snow-albedo feedback in higher elevation warming over the Himalayas, Tibetan Plateau and Central Asia, *Environ. Res. Lett.*, 9(11), doi:10.1088/1748-9326/9/11/114008, 2014.

Ginot, P., Dumont, M., Lim, S., Patris, N., Taupin, J. D., Wagnon, P., Gilbert, A., Arnaud, Y., Marinoni, A., Bonasoni, P. and Laj, P.: A 10 year record of black carbon and dust from a Mera Peak ice core (Nepal): Variability and potential impact on melting of Himalayan glaciers, *Cryosphere*, 8(4), 1479–1496, doi:10.5194/tc-8-1479-2014, 2014.

Ginoux, P., Chin, M., Tegen, I., Prospero, J. M., Holben, B., Dubovik, O. and Lin, S.-J.: Sources and distributions of dust aerosols simulated with the GOCART model, *J. Geophys. Res. Atmos.*, 106(D17), 20255–20273, doi:10.1029/2000JD000053, 2001.

Gustafson, W. I., Chapman, E. G., Ghan, S. J., Easter, R. C. and Fast, J. D.: Impact on modeled cloud characteristics due to simplified treatment of uniform cloud condensation nuclei during NEAQS 2004, *Geophys. Res. Lett.*, 34(19), doi:10.1029/2007GL030021, 2007.

Hadley, O. L. and Kirchstetter, T. W.: Black-carbon reduction of snow albedo, *Nat. Clim. Chang.*, 2(6), 437–440, doi:10.1038/nclimate1433, 2012.

Hansen, J. and Nazarenko, L.: Soot climate forcing via snow and ice albedos, *Proc. Natl. Acad. Sci.*, 101(2), 423–428, doi:10.1073/pnas.2237157100, 2004.

Hansen, J., Sato, M. and Ruedy, R.: Radiative forcing and climate response, *J. Geophys. Res. Atmos.*, 102(D6), 6831–6864, doi:10.1029/96JD03436, 1997.

He, C., Flanner, M. G., Chen, F., Barlage, M., Liou, K. N., Kang, S., Ming, J. and Qian, Y.: Black carbon-induced snow albedo reduction over the Tibetan Plateau: Uncertainties from snow grain shape and aerosol-snow mixing state based on an updated SNICAR model, *Atmos. Chem. Phys.*, 18(15), 11507–11527, doi:10.5194/acp-18-11507-2018, 2018.

Hess, M., Koepke, P. and Schult, I.: Optical Properties of Aerosols and Clouds: The Software

Package OPAC, *Bull. Am. Meteorol. Soc.*, 79(5), 831–844, doi:10.1175/1520-0477(1998)079<0831:OPOAAC>2.0.CO;2, 1998.

Holben, B. N., Eck, T. F., Slutsker, I., Tanré, D., Buis, J. P., Setzer, A., Vermote, E., Reagan, J. A., Kaufman, Y. J., Nakajima, T., Lavenu, F., Jankowiak, I. and Smirnov, A.: AERONET—A Federated Instrument Network and Data Archive for Aerosol Characterization, *Remote Sens. Environ.*, 66(1), 1–16, doi:10.1016/S0034-4257(98)00031-5, 1998.

Hu, Z., Zhao, C., Huang, J., Leung, L. R., Qian, Y., Yu, H., Huang, L. and Kalashnikova, O. V.: Trans-Pacific transport and evolution of aerosols: Evaluation of quasi-global WRF-Chem simulation with multiple observations, *Geosci. Model Dev.*, 9(5), 1725–1746, doi:10.5194/gmd-9-1725-2016, 2016.

Immerzeel, W. W., Van Beek, L. P. H. and Bierkens, M. F. P.: Climate change will affect the asian water towers, *Science* (80-.), 328(5984), 1382–1385, doi:10.1126/science.1183188, 2010.

IPCC: Climate change 2013: The physical science basis, *Contrib. Work. Gr. I to Fifth Assess. Rep. Intergov. Panel Clim. Chang.*, 33, doi:10.1017/CBO9781107415324, 2013.

Jacobi, H. W., Lim, S., Ménégos, M., Ginot, P., Laj, P., Bonasoni, P., Stocchi, P., Marinoni, A. and Arnaud, Y.: Black carbon in snow in the upper Himalayan Khumbu Valley, Nepal: Observations and modeling of the impact on snow albedo, melting, and radiative forcing, *Cryosphere*, 9(4), 1685–1699, doi:10.5194/tc-9-1685-2015, 2015.

Jayarathne, T., Stockwell, C. E., Bhave, P. V., Praveen, P. S., Rathnayake, C. M., Md Islam, R., Panday, A. K., Adhikari, S., Maharjan, R., Douglas Goetz, J., Decarlo, P. F., Saikawa, E., Yokelson, R. J. and Stone, E. A.: Nepal Ambient Monitoring and Source Testing Experiment (NAMaSTE): Emissions of particulate matter from wood-and dung-fueled cooking fires, garbage and crop residue burning, brick kilns, and other sources, *Atmos. Chem. Phys.*, 18(3), 2259–2286, doi:10.5194/acp-18-2259-2018, 2018.

Ji, Z. M.: Modeling black carbon and its potential radiative effects over the Tibetan Plateau, *Adv. Clim. Chang. Res.*, 7(3), 139–144, doi:10.1016/j.accre.2016.10.002, 2016.

Kaser, G., Grosshauser, M. and Marzeion, B.: Contribution potential of glaciers to water availability in different climate regimes, *Proc. Natl. Acad. Sci.*, 107(47), 20223–20227, doi:10.1073/pnas.1008162107, 2010.

Khan, A. A., Pant, N. C., Sarkar, A., Tandon, S. K., Thamban, M. and Mahalinganathan, K.: The Himalayan cryosphere: A critical assessment and evaluation of glacial melt fraction in the Bhagirathi basin, *Geosci. Front.*, 8(1), 107–115, doi:10.1016/j.gsf.2015.12.009, 2017.

Kopacz, M., Mauzerall, D. L., Wang, J., Leibensperger, E. M., Henze, D. K. and Singh, K.: Origin and radiative forcing of black carbon transported to the Himalayas and Tibetan Plateau, *Atmos. Chem. Phys.*, 11(6), 2837–2852, doi:10.5194/acp-11-2837-2011, 2011.

Kulkarni, A. V., Rathore, B. P. and Singh, S. K.: Distribution of seasonal snow cover in central and western Himalaya, *Ann. Glaciol.*, 51(54), 123–128, doi:10.3189/172756410791386445, 2010.

- Lau, K. M., Kim, M. K. and Kim, K. M.: Asian summer monsoon anomalies induced by aerosol direct forcing: The role of the Tibetan Plateau, *Clim. Dyn.*, 26(7–8), 855–864, doi:10.1007/s00382-006-0114-z, 2006.
- Lau, W. K. M., Kim, M. K., Kim, K. M. and Lee, W. S.: Enhanced surface warming and accelerated snow melt in the Himalayas and Tibetan Plateau induced by absorbing aerosols, *Environ. Res. Lett.*, 5(2), doi:10.1088/1748-9326/5/2/025204, 2010.
- Levy, R. C., Remer, L. A., Mattoo, S., Vermote, E. F. and Kaufman, Y. J.: Second-generation operational algorithm: Retrieval of aerosol properties over land from inversion of Moderate Resolution Imaging Spectroradiometer spectral reflectance, *J. Geophys. Res. Atmos.*, 112(13), doi:10.1029/2006JD007811, 2007.
- Levy, R. C., Remer, L. A., Kleidman, R. G., Mattoo, S., Ichoku, C., Kahn, R. and Eck, T. F.: Global evaluation of the Collection 5 MODIS dark-target aerosol products over land, *Atmos. Chem. Phys.*, 10(21), 10399–10420, doi:10.5194/acp-10-10399-2010, 2010.
- Li, Z., Lau, W. K. M., Ramanathan, V., Wu, G., Ding, Y., Manoj, M. G., Liu, J., Qian, Y., Li, J., Zhou, T., Fan, J., Rosenfeld, D., Ming, Y., Wang, Y., Huang, J., Wang, B., Xu, X., Lee, S. S., Cribb, M., Zhang, F., Yang, X., Zhao, C., Takemura, T., Wang, K., Xia, X., Yin, Y., Zhang, H., Guo, J., Zhai, P. M., Sugimoto, N., Babu, S. S. and Brasseur, G. P.: Aerosol and monsoon climate interactions over Asia, *Rev. Geophys.*, 54(4), 866–929, doi:10.1002/2015RG000500, 2016.
- Marcq, S., Laj, P., Roger, J. C., Villani, P., Sellegri, K., Bonasoni, P., Marinoni, A., Cristofanelli, P., Verza, G. P. and Bergin, M.: Aerosol optical properties and radiative forcing in the high Himalaya based on measurements at the Nepal Climate Observatory-Pyramid site (5079 m a.s.l.), *Atmos. Chem. Phys.*, 10(13), 5859–5872, doi:10.5194/acp-10-5859-2010, 2010.
- Ménégoz, M., Krinner, G., Balkanski, Y., Boucher, O., Cozic, A., Lim, S., Ginot, P., Laj, P., Gallée, H., Wagnon, P., Marinoni, A. and Jacobi, H. W.: Snow cover sensitivity to black carbon deposition in the Himalayas: From atmospheric and ice core measurements to regional climate simulations, *Atmos. Chem. Phys.*, 14(8), 4237–4249, doi:10.5194/acp-14-4237-2014, 2014.
- Menon, S., Koch, D., Beig, G., Sahu, S., Fasullo, J. and Orlikowski, D.: Black carbon aerosols and the third polar ice cap, *Atmos. Chem. Phys.*, 10(10), 4559–4571, doi:10.5194/acp-10-4559-2010, 2010.
- Ming, J., Cachier, H., Xiao, C., Qin, D., Kang, S., Hou, S. and Xu, J.: Black carbon record based on a shallow Himalayan ice core and its climatic implications, *Atmos. Chem. Phys.*, 8(5), 1343–1352, doi:10.5194/acp-8-1343-2008, 2008.
- Mlawer, E. J., Taubman, S. J., Brown, P. D., Iacono, M. J. and Clough, S. A.: Radiative transfer for inhomogeneous atmospheres: RRTM, a validated correlated-k model for the longwave, *J. Geophys. Res. Atmos.*, 102(D14), 16663–16682, doi:10.1029/97JD00237, 1997.
- Nair, V. S., Babu, S. S., Moorthy, K. K., Sharma, A. K., Marinoni, A. and Ajai: Black carbon aerosols over the Himalayas: Direct and surface albedo forcing, *Tellus, Ser. B Chem. Phys. Meteorol.*, 65(1), doi:10.3402/tellusb.v65i0.19738, 2013.

- Nakajima, T., Tonna, G., Rao, R., Boi, P., Kaufman, Y. and Holben, B.: Use of sky brightness measurements from ground for remote sensing of particulate polydispersions, *Appl. Opt.*, 35(15), 2672, doi:10.1364/AO.35.002672, 1996.
- Ningombam, S. S., Srivastava, A. K., Bagare, S. P., Singh, R. B., Kanawade, V. P. and Dorjey, N.: Assessment of aerosol optical and micro-physical features retrieved from direct and diffuse solar irradiance measurements from Skyradiometer at a high altitude station at Merak: Assessment of aerosol optical features from Merak, *Environ. Sci. Pollut. Res.*, 22(21), 16610–16619, doi:10.1007/s11356-015-4788-9, 2015.
- Niu, H., Kang, S., Wang, H., Zhang, R., Lu, X., Qian, Y., Paudyal, R., Wang, S., Shi, X. and Yan, X.: Seasonal variation and light absorption property of carbonaceous aerosol in a typical glacier region of the southeastern Tibetan Plateau, *Atmos. Chem. Phys.*, 18(9), 6441–6460, doi:10.5194/acp-18-6441-2018, 2018.
- Oleson, K. W., Lawrence, D. M., Gordon, B., Flanner, M. G., Kluzek, E., Peter, J., Levis, S., Swenson, S. C., Thornton, E. and Feddema, J.: Technical description of version 4.0 of the Community Land Model (CLM)., 2010.
- Painter, T. H., Rittger, K., McKenzie, C., Slaughter, P., Davis, R. E. and Dozier, J.: Retrieval of subpixel snow covered area, grain size, and albedo from MODIS, *Remote Sens. Environ.*, 113(4), 868–879, doi:10.1016/j.rse.2009.01.001, 2009.
- Painter, T. H., Bryant, A. C. and McKenzie Skiles, S.: Radiative forcing by light absorbing impurities in snow from MODIS surface reflectance data, *Geophys. Res. Lett.*, 39(17), doi:10.1029/2012GL052457, 2012.
- Painter, T. H., Seidel, F. C., Bryant, A. C., McKenzie Skiles, S. and Rittger, K.: Imaging spectroscopy of albedo and radiative forcing by light-absorbing impurities in mountain snow, *J. Geophys. Res. Atmos.*, 118(17), 9511–9523, doi:10.1002/jgrd.50520, 2013.
- Pfeffer, W. T., Arendt, A. A., Bliss, A., Bolch, T., Cogley, J. G., Gardner, A. S., Hagen, J. O., Hock, R., Kaser, G., Kienholz, C., Miles, E. S., Moholdt, G., Mölg, N., Paul, F., Radić, V., Rastner, P., Raup, B. H., Rich, J., Sharp, M. J., Andreassen, L. M., Bajracharya, S., Barrand, N. E., Beedle, M. J., Berthier, E., Bhambri, R., Brown, I., Burgess, D. O., Burgess, E. W., Cawkwell, F., Chinn, T., Copland, L., Cullen, N. J., Davies, B., De Angelis, H., Fountain, A. G., Frey, H., Giffen, B. A., Glasser, N. F., Gurney, S. D., Hagg, W., Hall, D. K., Haritashya, U. K., Hartmann, G., Herreid, S., Howat, I., Jiskoot, H., Khromova, T. E., Klein, A., Kohler, J., König, M., Kriegel, D., Kutuzov, S., Lavrentiev, I., Le Bris, R., Li, X., Manley, W. F., Mayer, C., Menounos, B., Mercer, A., Mool, P., Negrete, A., Nosenko, G., Nuth, C., Osmonov, A., Pettersson, R., Racoviteanu, A., Ranzi, R., Sarikaya, M. A., Schneider, C., Sigurdsson, O., Sirguey, P., Stokes, C. R., Wheate, R., Wolken, G. J., Wu, L. Z. and Wyatt, F. R.: The Randolph glacier inventory: A globally complete inventory of glaciers, *J. Glaciol.*, 60(221), 537–552, doi:10.3189/2014JoG13J176, 2014.
- Prasad, A. K., S. Yang, K. H., El-Askary, H. M. and Kafatos, M.: Melting of major Glaciers in the western Himalayas: Evidence of climatic changes from long term MSU derived tropospheric temperature trend (1979-2008), *Ann. Geophys.*, 27(12), 4505–4519, doi:10.5194/angeo-27-

4505-2009, 2009.

Qian, Y., Gong, D., Fan, J., Ruby Leung, L., Bennartz, R., Chen, D. and Wang, W.: Heavy pollution suppresses light rain in China: Observations and modeling, *J. Geophys. Res. Atmos.*, 114(15), doi:10.1029/2008JD011575, 2009.

Qian, Y., Flanner, M. G., Leung, L. R. and Wang, W.: Sensitivity studies on the impacts of Tibetan Plateau snowpack pollution on the Asian hydrological cycle and monsoon climate, *Atmos. Chem. Phys.*, 11(5), 1929–1948, doi:10.5194/acp-11-1929-2011, 2011.

Qian, Y., Wang, H., Zhang, R., Flanner, M. G. and Rasch, P. J.: A sensitivity study on modeling black carbon in snow and its radiative forcing over the Arctic and Northern China, *Environ. Res. Lett.*, 9(6), doi:10.1088/1748-9326/9/6/064001, 2014.

Qian, Y., Yasunari, T. J., Doherty, S. J., Flanner, M. G., Lau, W. K. M., Ming, J., Wang, H., Wang, M., Warren, S. G. and Zhang, R.: Light-absorbing particles in snow and ice: Measurement and modeling of climatic and hydrological impact, *Adv. Atmos. Sci.*, 32(1), 64–91, doi:10.1007/s00376-014-0010-0, 2015.

V. Ramanathan and G. Carmichael: Global and regional climate changes due to black carbon, *Nat. Geosci.*, 1(January), 221–227, doi:10.1038/ngeo156, 2008.

Ramanathan, V., Crutzen, P. J., Kiehl, J. T., Rosenfeld, D., Haywood, J., Boucher, O., Kaufman, Y. J., Collins, W. D., Hansen, J. E., Sato, M., Ruedy, R., Kiehl, J. T., Trenberth, K. E., Crutzen, P. J., Andreae, M. O., Charlson, R. J., Langner, J., Rodhe, H., Leovy, C. B., Warren, S. G., Clarke, A. D., Charlson, R. J., Grassl, H., Ogren, J. A., Charlson, R. J., Jayaraman, A., Satheesh, S. K., Ramanathan, V., Jacobson, M. J., Russell, P. B., Eck, T. F., Holben, B. N., Slutsker, I., Setzer, A., Raes, F., Bates, T., McGovern, F., Liedekerke, M. Van, Rajeev, K., Ramanathan, V., Meywerk, J., Lelieveld, J., Ramanathan, V., Konzelmann, T., Cahoon, D. R., Whitlock, C. H., Twomey, S., Novakov, T., Penner, J. E., Charlson, R. J., Martin, G. M., Johnson, W., Spice, A., Guillepe, I., Issac, G. A., Leaitch, W. R., Banic, C. M., Pawlowska, H., Brenguier, J.-L., Taylor, J. P., McHaffie, A., Coakley, J. A., Bernstein, R. L., Durkey, P. A., Kaufman, Y. J., Fraser, R. S., Nakajima, T., Higurashi, A., Kawamoto, K., Penner, J. E., Hansen, J., Sato, M., Ruedy, R., Lacis, A., Oinas, V., Warner, J. J., Rosenfeld, D., ____, ____, Rudich, Y., Lahav, R., Levitus, S., Stanhill, G., Cohen, S., Gilgen, H., Wild, M., Ohmura, A., Ramaswamy, V., Chen, C. T., Meehl, G. A., Washington, W. M., Erickson, D. J., Briegleb, B. P., Jaumann, P. J., Michell, J. F. B., Johns, T. C., Roeckner, E., Bengtsson, L., Feichter, J., et al.: Aerosols, climate, and the hydrological cycle., *Science*, 294(5549), 2119–24, doi:10.1126/science.1064034, 2001.

Ramanathan, V., Ramana, M. V., Roberts, G., Kim, D., Corrigan, C., Chung, C. and Winker, D.: Warming trends in Asia amplified by brown cloud solar absorption, *Nature*, 448(7153), 575–578, doi:10.1038/nature06019, 2007.

Ren, D. and Karoly, D.: Comparison of glacier-inferred temperatures with observations and climate model simulations, *Geophys. Res. Lett.*, 33(23), doi:10.1029/2006GL027856, 2006.

Ren, J., Jing, Z., Pu, J. and Qin, X.: Glacier variations and climate change in the central Himalaya over the past few decades, in *Annals of Glaciology*, vol. 43, pp. 218–222., 2006.

- Rittger, K., Painter, T. H. and Dozier, J.: Assessment of methods for mapping snow cover from MODIS, *Adv. Water Resour.*, 51, 367–380, doi:10.1016/j.advwatres.2012.03.002, 2013.
- Rittger, K., Bair, E. H., Kahl, A. and Dozier, J.: Spatial estimates of snow water equivalent from reconstruction, *Adv. Water Resour.*, 94, 345–363, doi:10.1016/j.advwatres.2016.05.015, 2016.
- Sarang, C., Tripathi, S. N., Kanawade, V. P., Koren, I. and Sivanand Pai, D.: Investigation of the aerosol-cloud-rainfall association over the Indian summer monsoon region, *Atmos. Chem. Phys.*, 17(8), doi:10.5194/acp-17-5185-2017, 2017.
- Schmale, J., Flanner, M., Kang, S., Sprenger, M., Zhang, Q., Guo, J., Li, Y., Schwikowski, M. and Farinotti, D.: Modulation of snow reflectance and snowmelt from Central Asian glaciers by anthropogenic black carbon, *Sci. Rep.*, 7, doi:10.1038/srep40501, 2017.
- Shrestha, A. B., Wake, C. P., Mayewski, P. A. and Dibb, J. E.: Maximum temperature trends in the Himalaya and its vicinity: An analysis based on temperature records from Nepal for the period 1971-94, *J. Clim.*, 12(9), 2775–2786, doi:10.1175/1520-0442(1999)012<2775:MTTITH>2.0.CO;2, 1999.
- Simard, M., Pinto, N., Fisher, J. B. and Baccini, A.: Mapping forest canopy height globally with spaceborne lidar, *J. Geophys. Res. Biogeosciences*, 116(4), doi:10.1029/2011JG001708, 2011.
- Singh, P. and Bengtsson, L.: Hydrological sensitivity of a large Himalayan basin to climate change, *Hydrol. Process.*, 18(13), 2363–2385, doi:10.1002/hyp.1468, 2004.
- Skiles, S. M., Painter, T. H., Deems, J. S., Bryant, A. C. and Landry, C. C.: Dust radiative forcing in snow of the Upper Colorado River Basin: 2. Interannual variability in radiative forcing and snowmelt rates, *Water Resour. Res.*, 48(7), doi:10.1029/2012WR011986, 2012.
- Svensson, J., Ström, J., Kivekäs, N., Dkhar, N. B., Tayal, S., Sharma, V. P., Jutila, A., Backman, J., Virkkula, A., Ruppel, M., Hyvärinen, A., Kontu, A., Backman, J., Leppäranta, M., Hooda, R. K., Korhola, A., Asmi, E. and Lihavainen, H.: Light-Absorption of dust and elemental carbon in snow in the Indian Himalayas and the Finnish Arctic, *Atmos. Meas. Tech.*, 11(3), 1403–1416, doi:10.5194/amt-11-1403-2018, 2018.
- Thind, P. S., Chandel, K. K., Sharma, S. K., Mandal, T. K. and John, S.: Light-absorbing impurities in snow of the Indian Western Himalayas: impact on snow albedo, radiative forcing, and enhanced melting, *Environ. Sci. Pollut. Res.*, 26(8), 7566–7578, doi:10.1007/s11356-019-04183-5, 2019.
- Toon, O. B., McKay, C. P., Ackerman, T. P. and Santhanam, K.: Rapid calculation of radiative heating rates and photodissociation rates in inhomogeneous multiple scattering atmospheres, *J. Geophys. Res.*, 94(D13), 16287, doi:10.1029/JD094iD13p16287, 1989.
- Tripathi, S. N., Dey, S., Chandel, A., Srivastava, S., Singh, R. P. and Holben, B. N.: Comparison of MODIS and AERONET derived aerosol optical depth over the Ganga Basin, India, *Ann. Geophys.*, 23(4), 1093–1101, doi:10.5194/angeo-23-1093-2005, 2005.
- Wake, C. P., Mayewski, P. A., Li, Z., Han, J. and Qin, D.: Modern eolian dust deposition in central

- Asia, *Tellus B Chem. Phys. Meteorol.*, 46(3), 220–233, doi:10.3402/tellusb.v46i3.15793, 1994.
- Wang, B., Bao, Q., Hoskins, B., Wu, G. and Liu, Y.: Tibetan Plateau warming and precipitation changes in East Asia, *Geophys. Res. Lett.*, 35(14), doi:10.1029/2008GL034330, 2008.
- Wang, M., Xu, B., Cao, J., Tie, X., Wang, H., Zhang, R., Qian, Y., Rasch, P. J., Zhao, S., Wu, G., Zhao, H., Joswiak, D. R., Li, J. and Xie, Y.: Carbonaceous aerosols recorded in a southeastern Tibetan glacier: Analysis of temporal variations and model estimates of sources and radiative forcing, *Atmos. Chem. Phys.*, 15(3), 1191–1204, doi:10.5194/acp-15-1191-2015, 2015.
- Warren, S. G.: Can black carbon in snow be detected by remote sensing?, *J. Geophys. Res. Atmos.*, 118(2), 779–786, doi:10.1029/2012JD018476, 2013.
- Warren, S. G. and Wiscombe, W. J.: A Model for the Spectral Albedo of Snow. II: Snow Containing Atmospheric Aerosols, *J. Atmos. Sci.*, 37(12), 2734–2745, doi:10.1175/1520-0469(1980)037<2734:AMFTSA>2.0.CO;2, 1980.
- Van Der Werf, G. R., Randerson, J. T., Giglio, L., Collatz, G. J., Mu, M., Kasibhatla, P. S., Morton, D. C., Defries, R. S., Jin, Y. and Van Leeuwen, T. T.: Global fire emissions and the contribution of deforestation, savanna, forest, agricultural, and peat fires (1997–2009), *Atmos. Chem. Phys.*, 10(23), 11707–11735, doi:10.5194/acp-10-11707-2010, 2010.
- Xu, B., Cao, J., Hansen, J., Yao, T., Joswia, D. R., Wang, N., Wu, G., Wang, M., Zhao, H., Yang, W., Liu, X. and He, J.: Black soot and the survival of Tibetan glaciers, *Proc. Natl. Acad. Sci.*, 106(52), 22114–22118, doi:10.1073/pnas.0910444106, 2009a.
- Xu, J., Grumbine, R. E., Shrestha, A., Eriksson, M., Yang, X., Wang, Y. and Wilkes, A.: The melting Himalayas: Cascading effects of climate change on water, biodiversity, and livelihoods, *Conserv. Biol.*, 23(3), 520–530, doi:10.1111/j.1523-1739.2009.01237.x, 2009b.
- Yao, T., Pu, J., Lu, A., Wang, Y. and Yu, W.: Recent Glacial Retreat and Its Impact on Hydrological Processes on the Tibetan Plateau, China, and Surrounding Regions, *Arctic, Antarct. Alp. Res.*, 39(4), 642–650, doi:10.1657/1523-0430(07-510)[YAO]2.0.CO;2, 2007.
- Yasunari, T. J., Bonasoni, P., Laj, P., Fujita, K., Vuillermoz, E., Marinoni, A., Cristofanelli, P., Duchi, R., Tartari, G. and Lau, K. M.: Estimated impact of black carbon deposition during pre-monsoon season from Nepal Climate Observatory - Pyramid data and snow albedo changes over Himalayan glaciers, *Atmos. Chem. Phys.*, 10(14), 6603–6615, doi:10.5194/acp-10-6603-2010, 2010a.
- Yasunari, T. J., Bonasoni, P., Laj, P., Fujita, K., Vuillermoz, E., Marinoni, A., Cristofanelli, P., Duchi, R., Tartari, G. and Lau, K.-M.: Preliminary estimation of black carbon deposition from Nepal Climate Observatory-Pyramid data and its possible impact on snow albedo changes over Himalayan glaciers during the pre-monsoon season., *Atmos. Chem. Phys. Discuss.*, 10(4), 9291–9328 [online] Available from: <https://ezp.lib.unimelb.edu.au/login?url=https://search.ebscohost.com/login.aspx?direct=true&db=eih&AN=51503391&site=eds-live&scope=site>, 2010b.
- Yasunari, T. J., Tan, Q., Lau, K. M., Bonasoni, P., Marinoni, A., Laj, P., Ménégoz, M., Takemura, T.

- and Chin, M.: Estimated range of black carbon dry deposition and the related snow albedo reduction over Himalayan glaciers during dry pre-monsoon periods, *Atmos. Environ.*, 78, 259–267, doi:10.1016/j.atmosenv.2012.03.031, 2013.
- Zaveri, R. A. and Peters, L. K.: A new lumped structure photochemical mechanism for large-scale applications, *J. Geophys. Res. Atmos.*, 104(D23), 30387–30415, doi:10.1029/1999JD900876, 1999.
- Zaveri, R. A., Easter, R. C., Fast, J. D. and Peters, L. K.: Model for Simulating Aerosol Interactions and Chemistry (MOSAIC), *J. Geophys. Res. Atmos.*, 113(13), doi:10.1029/2007JD008782, 2008.
- Zhang, Q., Streets, D. G., Carmichael, G. R., He, K. B., Huo, H., Kannari, A., Klimont, Z., Park, I. S., Reddy, S., Fu, J. S., Chen, D., Duan, L., Lei, Y., Wang, L. T. and Yao, Z. L.: Asian emissions in 2006 for the NASA INTEX-B mission, *Atmos. Chem. Phys.*, 9(14), 5131–5153, doi:10.5194/acp-9-5131-2009, 2009.
- Zhang, R., Wang, H., Qian, Y., Rasch, P. J., Easter, R. C., Ma, P. L., Singh, B., Huang, J. and Fu, Q.: Quantifying sources, transport, deposition, and radiative forcing of black carbon over the Himalayas and Tibetan Plateau, *Atmos. Chem. Phys.*, 15(11), 6205–6223, doi:10.5194/acp-15-6205-2015, 2015.
- Zhang, Y., Kang, S., Sprenger, M., Cong, Z., Gao, T., Li, C., Tao, S., Li, X., Zhong, X., Xu, M., Meng, W., Neupane, B., Qin, X. and Sillanpää, M.: Black carbon and mineral dust in snow cover on the Tibetan Plateau, *Cryosph.*, 12(2), 413–431, doi:10.5194/tc-12-413-2018, 2018.
- Zhao, C., Liu, X., Leung, L. R. and Hagos, S.: Radiative impact of mineral dust on monsoon precipitation variability over West Africa, *Atmos. Chem. Phys.*, 11(5), 1879–1893, doi:10.5194/acp-11-1879-2011, 2011.
- Zhao, C., Leung, L. R., Easter, R., Hand, J. and Avise, J.: Characterization of speciated aerosol direct radiative forcing over California, *J. Geophys. Res. Atmos.*, 118(5), 2372–2388, doi:10.1029/2012JD018364, 2013a.
- Zhao, C., Chen, S., Leung, L. R., Qian, Y., Kok, J. F., Zaveri, R. A. and Huang, J.: Uncertainty in modeling dust mass balance and radiative forcing from size parameterization, *Atmos. Chem. Phys.*, 13(21), 10733–10753, doi:10.5194/acp-13-10733-2013, 2013b.
- Zhao, C., Hu, Z., Qian, Y., Ruby Leung, L., Huang, J., Huang, M., Jin, J., Flanner, M. G., Zhang, R., Wang, H., Yan, H., Lu, Z. and Streets, D. G.: Simulating black carbon and dust and their radiative forcing in seasonal snow: A case study over North China with field campaign measurements, *Atmos. Chem. Phys.*, 14(20), 11475–11491, doi:10.5194/acp-14-11475-2014, 2014.